Supporting information

Synthesis and Electrocatalytic Property of Diiron Hydride Complexes Derived from a Thiolate-bridged Diiron Complex

Dawei Yang, Yang Li, Baomin Wang, Xiangyu Zhao, Linan Su, Si Chen, Peng Tong, Yi Luo and Jingping Qu*

S*tate Key Laboratory of Fine Chemicals, School of Pharmaceutical Science and Technology, Faculty of Chemical, Environmental and Biological Science and Technology, Dalian University of Technology, 2 Linggong Road, Dalian 116024, P. R. China.*

*E-mail: qujp@dlut.edu.cn

Contents:

Table S1. Crystallographic data for **1[BF_4]**, **4**

	1[BF_4]	**4**
Formula	$C_{26}H_{34}Fe_2S_2BF_4$	$C_{26}H_{35}Fe_2S_2$
Formula weight	609.16	523.36
Crystal dimensions (mm^3)	0.27 × 0.22 × 0.19	0.40 × 0.30 × 0.20
Crystal system	Orthorhombic	Triclinic
Space group	Cmca	P−1
a (Å)	15.566(4)	9.6939(12)
b (Å)	26.416(6)	9.8146(13)
c (Å)	13.530(3)	15.4150(19)
α (deg)	90.00	104.461(9)
β (deg)	90.00	100.202(9)
γ (deg)	90.00	108.604(9)
Volume ($Å^3$)	5563(2)	1292.2(3)
Z	8	2
T (K)	298(2)	220(2)
D_{calcd} ($g\ cm^{-3}$)	1.455	1.345
μ (mm^{-1})	1.233	1.295
F (000)	2520	550
No. of rflns. collected	14942	11884
No. of indep. rflns. /R_{int}	2554 / 0.0374	4442 / 0.0617
No. of obsd. rflns. [$I_0 > 2\sigma(I_0)$]	1889	2526
Data / restraints / parameters	2554 / 230 / 266	4442 / 240 / 274
R_1 / wR_2 [$I_0 > 2\sigma(I_0)$][a]	0.0421 / 0.1309	0.0590 / 0.1383
R_1 / wR_2 (all data)[a]	0.0614 / 0.1454	0.1127 / 0.1553
GOF (on F^2)[a]	1.000	1.050
Largest diff. peak and hole (e $Å^{-3}$)	0.553 / –0.328	0.850 / –0.421

Table S2. Crystallographic data for **5**, **7[BF_4]**

	5	**7[BF_4]**
Formula	$C_{26}H_{34}Ru_2S_2$	$C_{26}H_{35}BF_4Ru_2S_2$
Formula weight	612.79	700.61
Crystal dimensions (mm^3)	0.32 × 0.25 × 0.21	0.45 × 0.33 × 0.31
Crystal system	Triclinic	Monoclinic
Space group	P−1	$P2_1/c$
a (Å)	10.9904(7)	14.6275(12)
b (Å)	15.3232(10)	27.412(2)
c (Å)	16.1802(10)	15.5093(13)
α (deg)	85.717(4)	90.00
β (deg)	80.189(4)	115.1470(10)
γ (deg)	69.812(4)	90.00
Volume (Å ^{3})	2519.7(3)	5629.4(8)
Z	4	8
T (K)	298(2)	298(2)
D_{calcd} ($g\ cm^{-3}$)	1.615	1.653
μ (mm^{-1})	1.375	1.262
F (000)	1240	2816
No. of rflns. collected	23379	25591
No. of indep. rflns. /R_{int}	8843 / 0.0305	9901 / 0.0278
No. of obsd. rflns. [$I_0 > 2\sigma(I_0)$]	7067	8184
Data / restraints / parameters	8843 / 6 / 509	9901 / 102 / 685
R_1 / wR_2 [$I_0 > 2\sigma(I_0)$][a]	0.0611 / 0.1835	0.0330 / 0.0835
R_1 / wR_2 (all data)[a]	0.0752 / 0.1920	0.0435 / 0.0883
GOF (on F^2)[a]	1.000	1.018
Largest diff. peak and hole (e Å $^{-3}$)	1.920 / –1.763	0.824 / –0.411

Table S3. Crystallographic data for **8[BF_4]**

	8[BF_4]
Formula	$C_{26}H_{34}BF_4FeRuS_2$
Formula weight	654.38
Crystal dimensions (mm^3)	0.30 × 0.27 × 0.25
Crystal system	Orthorhombic
Space group	Cmca
a (Å)	15.595(14)
b (Å)	26.18(2)
c (Å)	13.761(11)
α (deg)	90.00
β (deg)	90.00
γ (deg)	90.00
Volume (Å ^{3})	5618(8)
Z	8
T (K)	298(2)
D_{calcd} (g cm^{-3})	1.547
μ (mm^{-1})	1.243
F (000)	2664
No. of rflns. collected	14547
No. of indep. rflns. /R_{int}	2557/0.1072
No. of obsd. rflns. [$I_0 > 2\sigma(I_0)$]	1348
Data / restraints / parameters	2557 / 61 / 168
R_1 / wR_2 [$I_0 > 2\sigma(I_0)$][a]	0.0861 / 0.1775
R_1 / wR_2 (all data)[a]	0.1387 / 0.1933
GOF (on F^2)[a]	0.989
Largest diff. peak and hole (e Å $^{-3}$)	1.044 / –0.932

Figure S1. ORTEP diagram of **1[BF_4]**

Hydrogen atoms and counteranion BF_4^- are omitted for clarity (thermal ellipsoids shown at 30% probability)

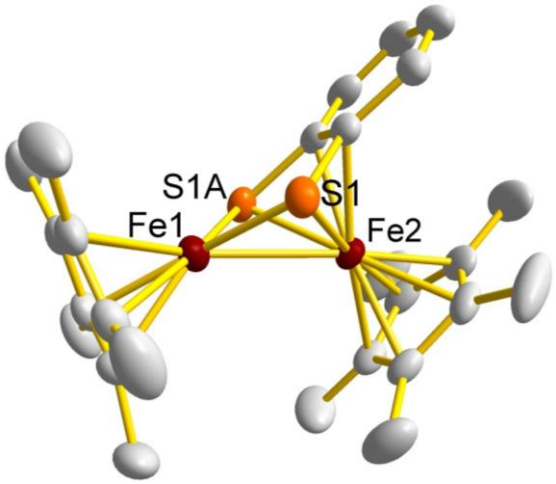

Table S4. Selected bond distances (Å) and bond angles (deg) for **1[BF_4]**

Distances (Å)			
Fe1–Fe2	2.680(1)	Fe2–S1	2.270(1)
Fe1–S1	2.171(1)	Fe2–C13	2.140(3)
C13–C13A	1.404(8)	Fe1–Cp*1	1.756(1)
Fe2–Cp*2	1.684(1)		
Angles (deg)			
Fe1–S1–Fe2	74.19(3)	S1–Fe1–S2	91.33(6)
S1–Fe2–S1A	86.30(3)	Fe2–Fe1–S1	54.60(2)
Fe1–Fe2–S1	51.21(2)	Fe2–S1–C13	62.61(1)
Torsion angles (deg)			
S1–Fe1Fe2–S1A	122.67(4)	Fe1–S1S1A–Fe2	115.15(5)
Fe1–S1S1A–C13	13.42(1)	Cp*1–Cp*2	60.4(4)

Figure S2. ORTEP diagram of **4**

Hydrogen atoms except for the bridging hydrogen between two Fe atoms are omitted for clarity (thermal ellipsoids shown at 30% probability)

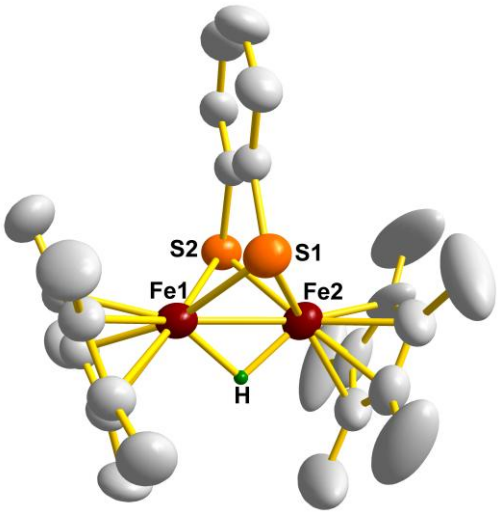

Table S5. Selected bond distances (Å) and bond angles (deg) for **4**

Distances (Å)			
Fe1–Fe2	2.4159(13)	Fe1–H	1.58(6)
Fe2–H	1.62(5)	Fe1–S1	2.2671(19)
Fe1–S2	2.2803(18)	Fe2–S1	2.2609(17)
Fe2–S2	2.2649(18)	Fe1–Cp*1	1.6967(9)
Fe2–Cp*2	1.6989(7)		
Angles (deg)			
Fe1–S1–Fe2	64.49(5)	Fe1–S2–Fe2	64.22(5)
S1–Fe2–Fe1	57.88(5)	S2–Fe1–Fe2	57.58(5)
S2–Fe2–Fe1	58.20(5)	S1–Fe2–S2	81.16(6)
S1–Fe1–S2	80.69(6)	S1–Fe1–Fe2	57.63(5)
Torsion angles (deg)			
S1–Fe1Fe2–S2	100.13(8)	Cp*1–Cp*2	43.8(3)

Figure S3. ORTEP diagram of **5**

One of the two crystallographically independent molecules is shown. Hydrogen atoms are omitted for clarity (thermal ellipsoids shown at 30% probability)

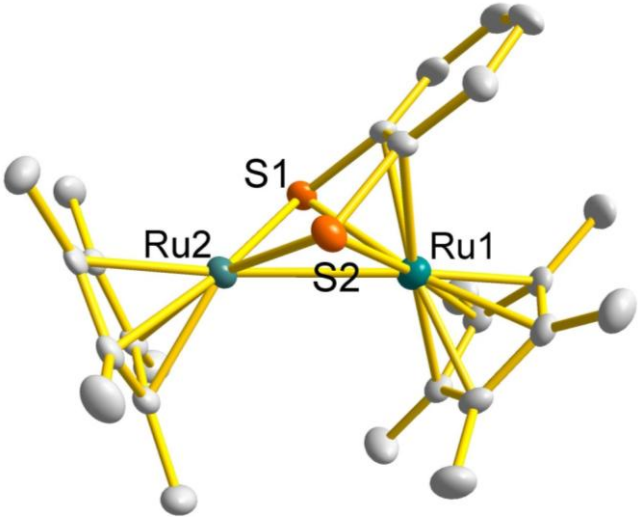

Table S6. Selected bond distances (Å) and bond angles (deg) for **5**

	Molecule 1	Molecule 2		Molecule 1	Molecule 2
Distances (Å)					
Ru1–Ru2	2.8335(10)	2.8472(10)	Ru1–S1	2.332(2)	2.341(2)
Ru1–S2	2.333 (2)	2.341(2)	Ru2–S1	2.204(2)	2.219 (2)
Ru2–S2	2.212(2)	2.214 (2)	Ru1–C21	2.133(7)	2.167(7)
Ru1–C22	2.152(7)	2.163(7)	S1–C21	1.751(8)	1.781(8)
S2–C22	1.773(8)	1.763(7)	C21–C22	1.422(12)	1.426(12)
C22–C23	1.410(11)	1.411(11)	C23–C24	1.355(16)	1.345(14)
C24–C25	1.392(17)	1.404(16)	C25–C26	1.365(16)	1.351(15)
C26–C21	1.430(12)	1.413(11)	Ru1–Cp*1	1.7041(9)	1.7094(8)
Ru2–Cp*2	1.7432(7)	1.7346(7)			
Angles (deg)					
Ru1–S1–Ru2	77.25(6)	77.23(6)	Ru1–S2–Ru2	77.08(7)	77.32(6)
Ru2–Ru1–S1	49.35(5)	49.48(5)	Ru1–Ru2–S1	53.40(6)	53.30(6)
Ru2–Ru1–S2	49.54(5)	49.34(5)	Ru1–Ru2–S2	53.38(5)	53.34(5)
S1–Ru1–S2	82.61(7)	82.31(7)	S1–Ru2–S2	88.43(8)	88.05(7)
Ru2–S1–C21	107.2(3)	107.1(3)	Ru2–S2–C22	106.8(3)	107.7(3)
Ru1–S1–C21	61.0(2)	61.7(2)	Ru1–S2–C22	61.4(2)	61.7(2)
Ru2–Ru1–C21	78.7(2)	78.8(2)	Ru2–Ru1–C22	78.85(19)	78.7(2)
C21–Ru1–C22	38.8(3)	38.5(3)			
Torsion angles (deg)					
S1–Ru1Ru2–S2	120.6(1)	120.1(1)	Ru1–S1S2–Ru2	116.25(9)	115.97(9)
Cp*1–Cp*2	64.6(2)	64.2(2)			

Figure S4. ORTEP diagram of **7[BF_4]**

One of the two crystallographically independent molecules is shown. The BF_4^- anion and hydrogen atoms except for the bridging hydrogen between two Ru atoms are omitted for clarity (thermal ellipsoids shown at 30% probability)

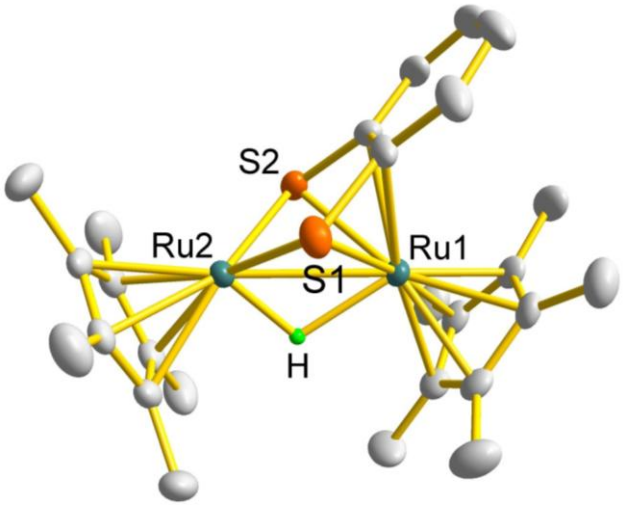

Table S7. Selected bond distances (Å) and bond angles (deg) for **7[BF_4]**

	Molecule 1	Molecule 2		Molecule 1	Molecule 2
Distances (Å)					
Ru1–Ru2	2.8033(4)	2.8190(4)	Ru1–S1	2.4393(10)	2.4479(10)
Ru1–S2	2.4423(9)	2.4382(11)	Ru2–S1	2.2894(10)	2.2809(11)
Ru2–S2	2.2782(10)	2.2819(10)	Ru1–C21	2.307(3)	2.295(4)
Ru1–C22	2.311(4)	2.299(4)	S1–C21	1.758(4)	1.762(4)
S2–C22	1.765(4)	1.756(5)	C21–C22	1.406(5)	1.405(6)
C22–C23	1.419(5)	1.430(6)	C23–C24	1.359(6)	1.344(9)
C24–C25	1.394(6)	1.378(9)	C25–C26	1.356(6)	1.370(8)
C26–C21	1.421(5)	1.414(6)	Ru1–Cp*1	1.8187(3)	1.8231(3)
Ru2–Cp*2	1.8278(3)	1.8320(3)			
Angles (deg)					
Ru1–S1–Ru2	72.64(3)	73.09(3)	Ru1–S2–Ru2	72.77(3)	73.26(3)
Ru2–Ru1–S1	51.21(2)	50.73(3)	Ru1–Ru2–S1	56.15(2)	56.18(3)
Ru2–Ru1–S2	50.91(2)	50.82(2)	Ru1–Ru2–S2	56.32(2)	55.92(3)
S1–Ru1–S2	79.93(3)	79.79(4)	S1–Ru2–S2	86.71(3)	86.75(4)
Ru1–S1–C21	64.29(12)	63.64(13)	Ru1–S2–C22	64.30(12)	64.09(13)
Ru2–S1–C21	107.04(13)	106.92(17)	Ru2–S2–C22	107.19(13)	107.17(16)
Ru2–Ru1–C21	78.91(9)	78.55(9)	Ru2–Ru1–C22	78.79(9)	78.54(10)
C21–Ru1–C22	35.46(13)	35.62(16)			
Torsion angles (deg)					
S1–Ru1Ru2–S2	111.342(45)	111.775(51)	Ru1–S1S2–Ru2	104.938(40)	105.716(45)
Cp*1–Cp*2	64.1(2)	63.4(2)			

Figure S5. ORTEP diagram of **8[BF_4]**

Hydrogen atoms and counteranion BF_4^- are omitted for clarity (thermal ellipsoids shown at 30% probability)

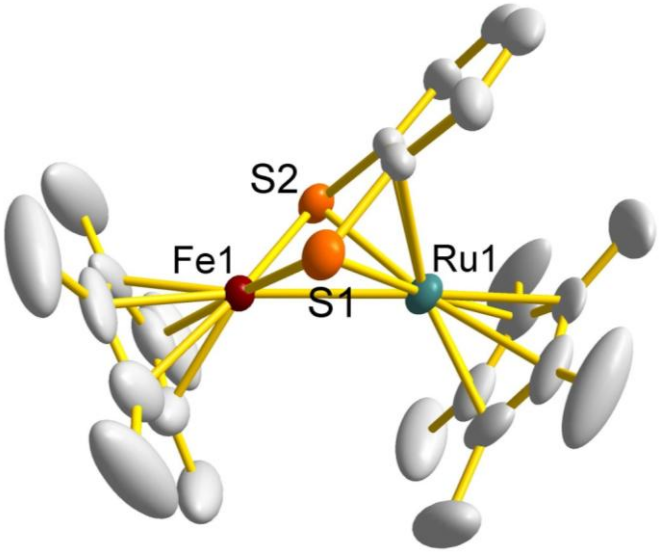

Table S8. Selected bond distances (Å) and bond angles (deg) for **8[BF_4]**

Distances (Å)			
Fe1–Ru1	2.690(3)	Fe1–S1	2.179(4)
Ru1–S1	2.412(3)	Ru1–C21	2.257(10)
C21–C21’	1.43(2)		
Angles (deg)			
Fe1–S1–Ru1	71.54(11)	S1–Fe1–S1’	91.7(2)
S1–Ru1–S1’	80.8(2)	Ru1–Fe1–S1	58.25(9)
Fe1–Ru1–S1	50.21(9)	Ru1–S1–C21	63.7(4)
Torsion angles (deg)			
S1–Fe1Ru1–S1’	115.02(15)	Fe1–S1S1’–Ru1	106.24(15)
Fe1–S1S1’–C21	174.5(4)	Cp*1–Cp*2	61.1(7)

Figure S6. ESI-HRMS of **3[BF$_4$]** in CH_2Cl_2

(a) The signal at an m/z = 523.0873 corresponds to [**3**]$^+$. (b) Calculated isotopic distribution for [**3**]$^+$ (upper) and the amplifying experimental diagram for [**3**]$^+$ (bottom).

(a)

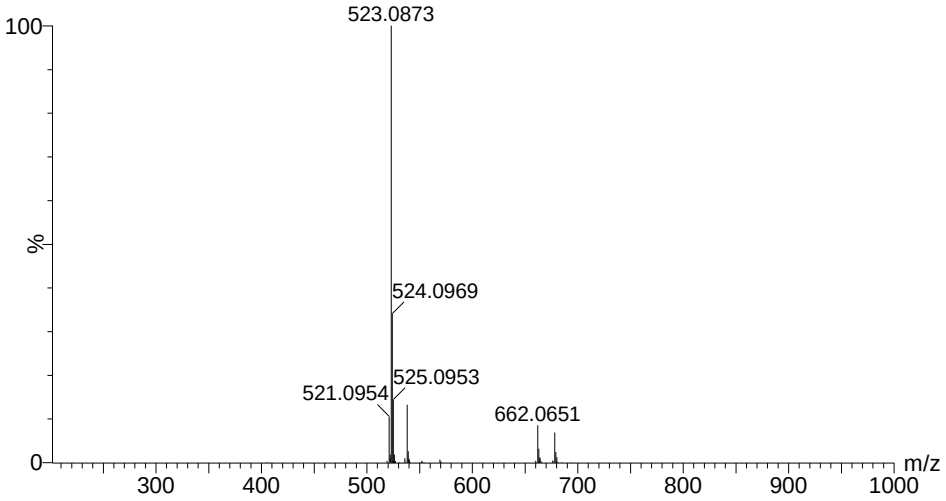

(b)

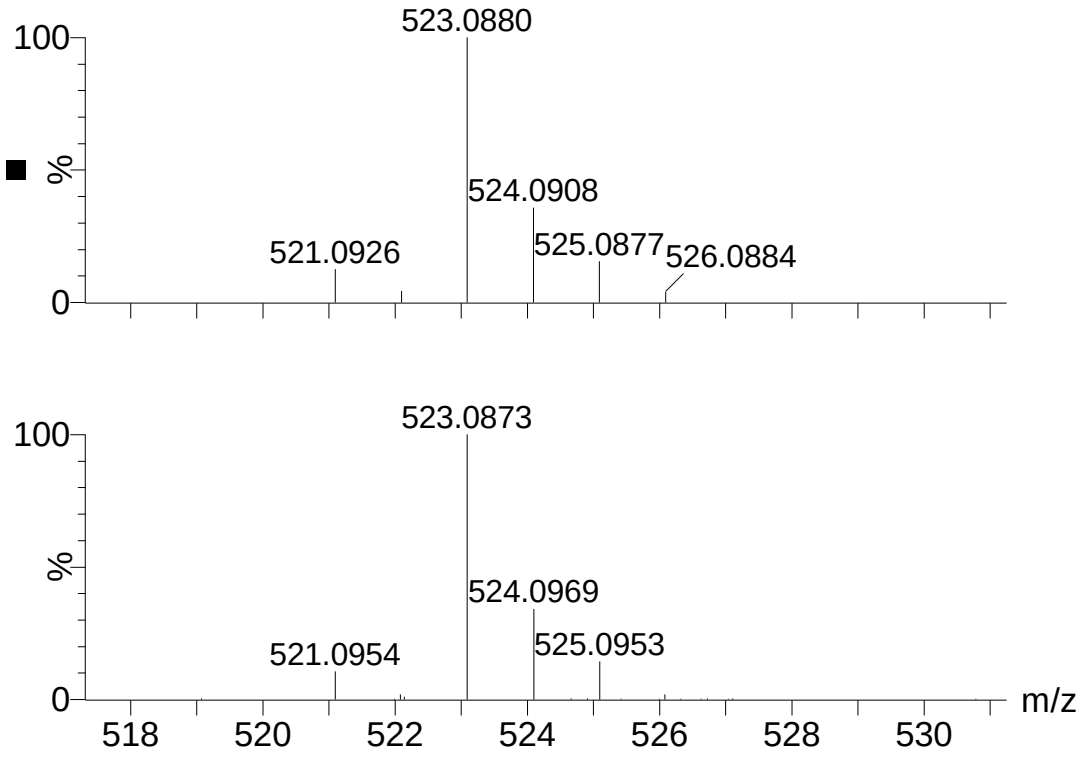

Figure S7. ESI-HRMS of **3[BPh$_4$]** in CH_2Cl_2

(a) The signal at an m/z = 523.0876 corresponds to $[\mathbf{3}]^+$. (b) Calculated isotopic distribution for $[\mathbf{3}]^+$ (upper) and the amplifying experimental diagram for $[\mathbf{3}]^+$ (bottom).

(a)

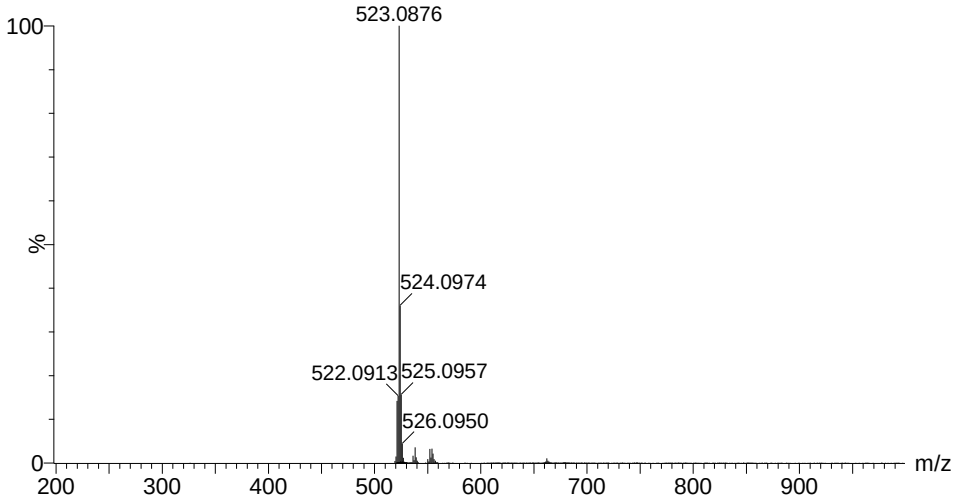

(b)

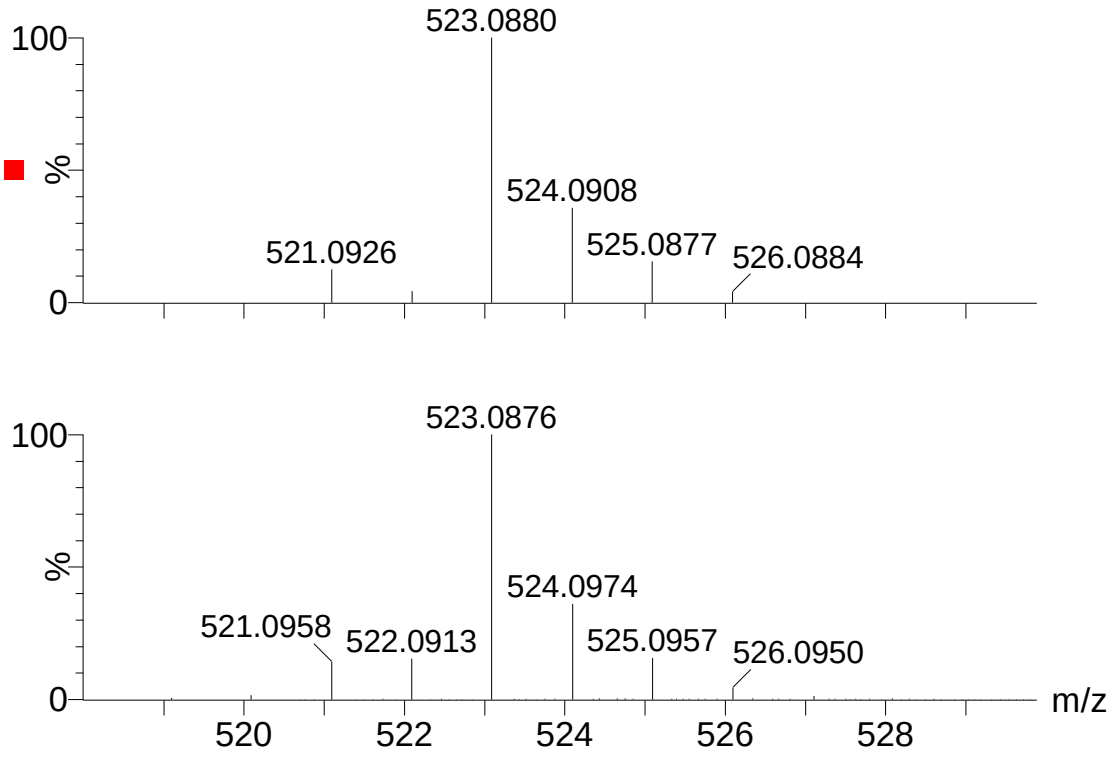

Figure S8. ESI-HRMS of **3[BAr$^{F}_{4}$]** in CH_2Cl_2

(a) The signal at an m/z = 523.0879 corresponds to $[\mathbf{3}]^+$ (b) Calculated isotopic distribution for $[\mathbf{3}]^+$ (upper) and the amplifying experimental diagram for $[\mathbf{3}]^+$ (bottom).

(a)

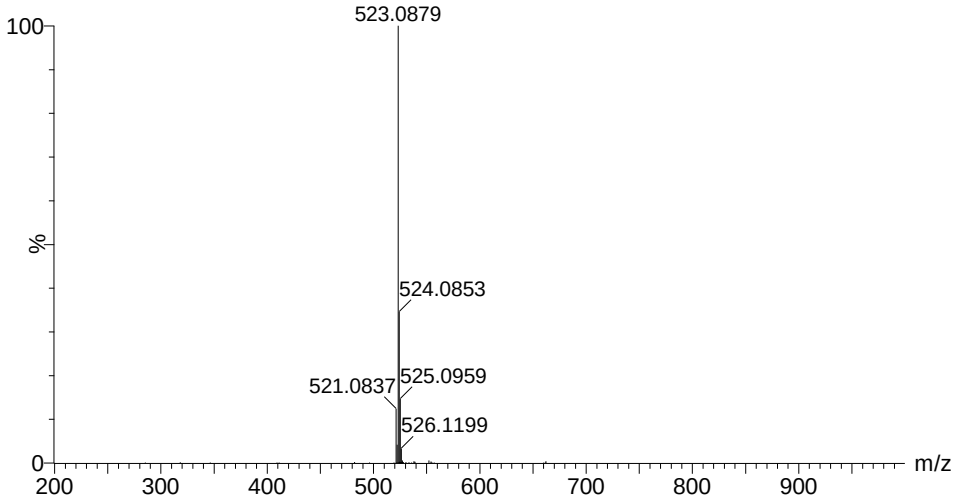

(b)

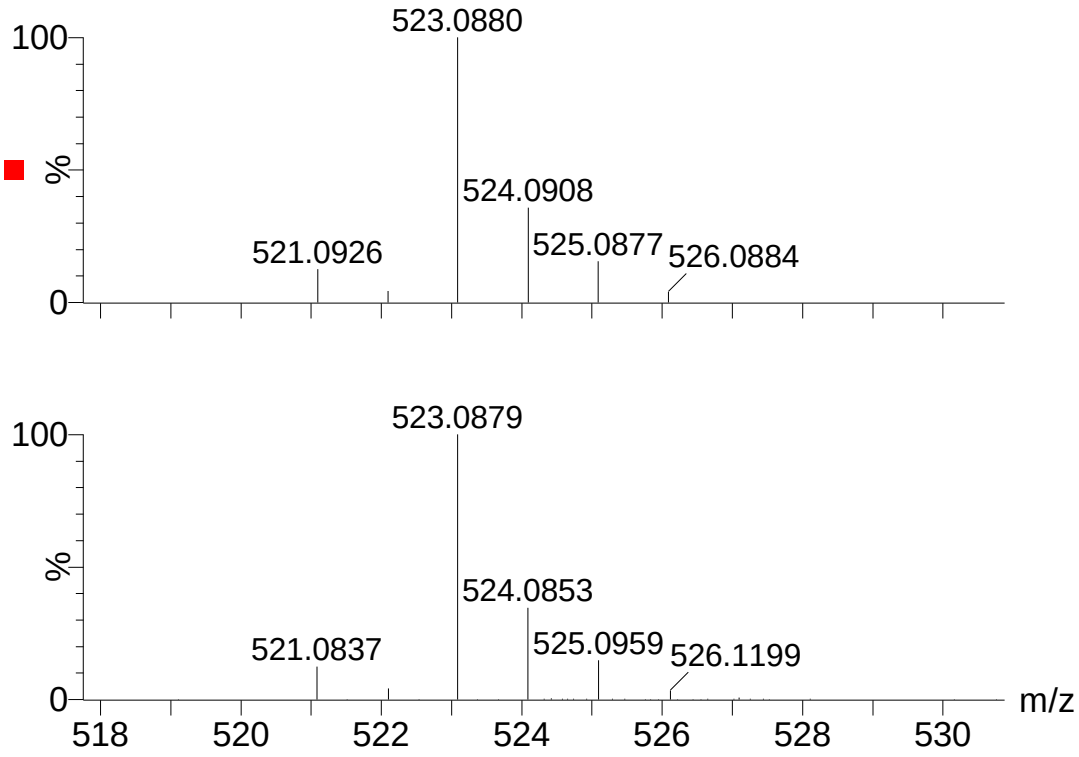

Figure S9. ESI-HRMS of **7[BF_4]** in CH_2Cl_2

(a) The signal at an m/z = 615.0246 corresponds to [**7**]$^+$ (b) Calculated isotopic distribution for [**7**]$^+$ (upper) and the amplifying experimental diagram for [**7**]$^+$ (bottom).

(a)

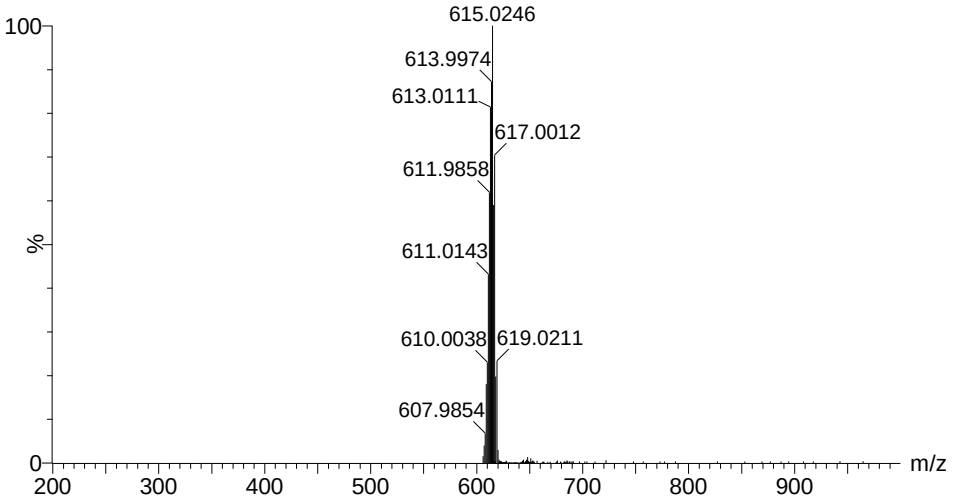

(b)

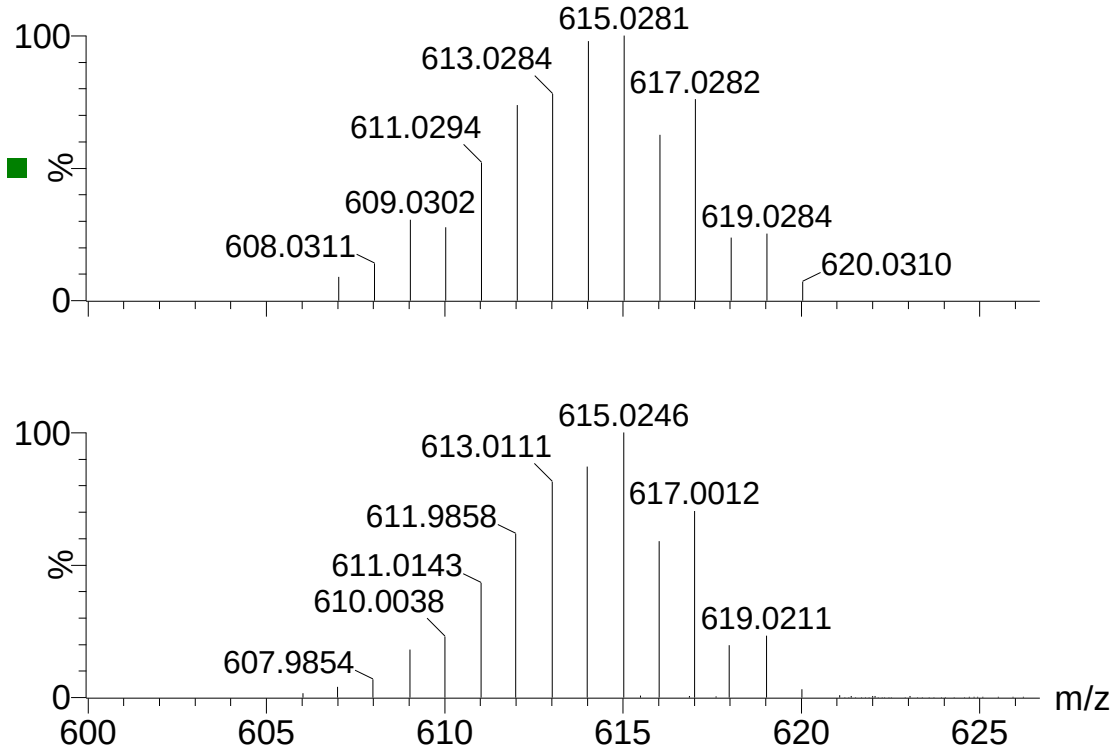

Figure S10. ESI-HRMS of **8[BF$_4$]** in CH_2Cl_2

(a) The signal at an m/z = 568.0483 corresponds to [**8**]$^+$ (b) Calculated isotopic distribution for [**8**]$^+$ (upper) and the amplifying experimental diagram for [**8**]$^+$ (bottom).

(a)

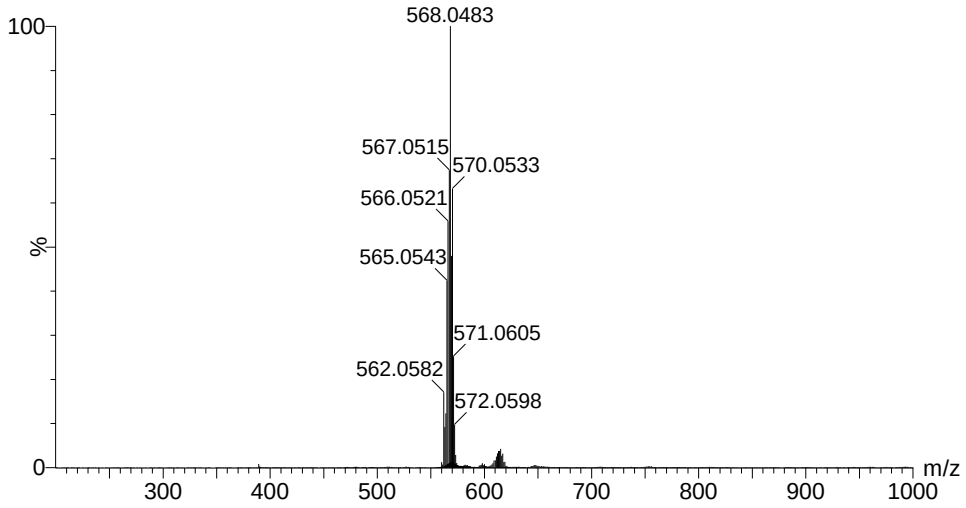

(b)

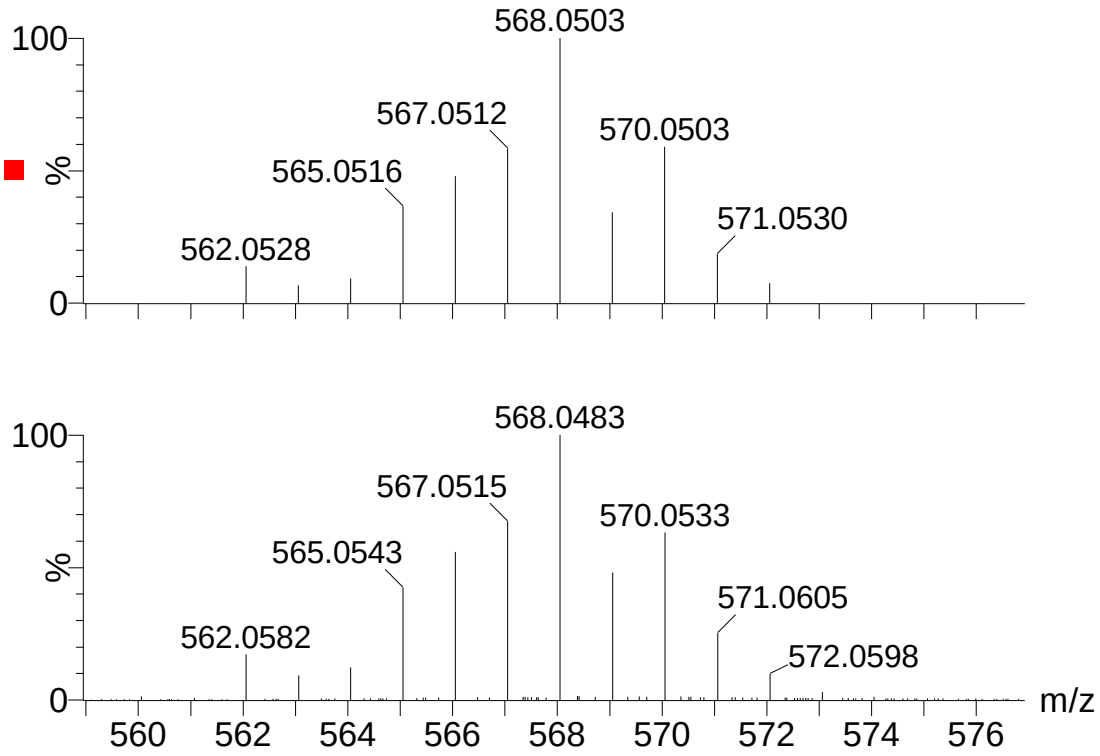

Figure S11. The ^{1}H NMR spectrum of **1[BF$_4$]** in CD_2Cl_2

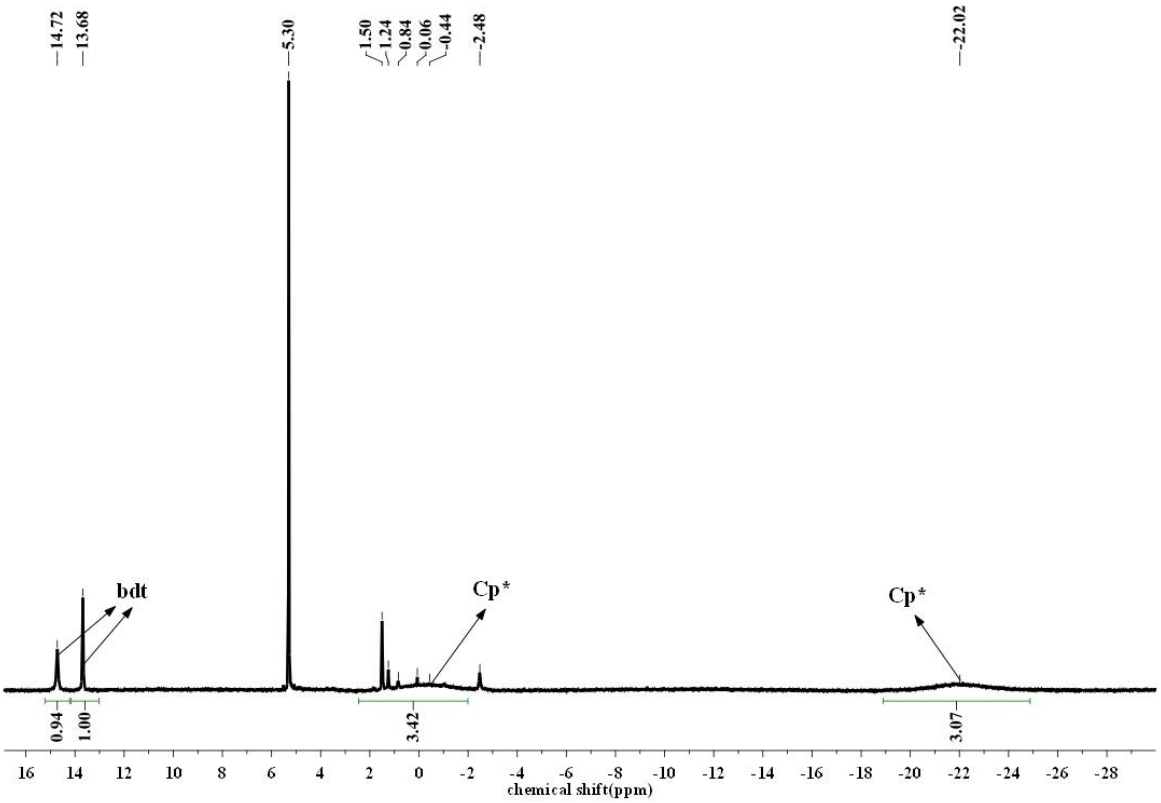

Figure S12. The ^{1}H NMR spectrum of **3[BF$_4$]** in CD_2Cl_2

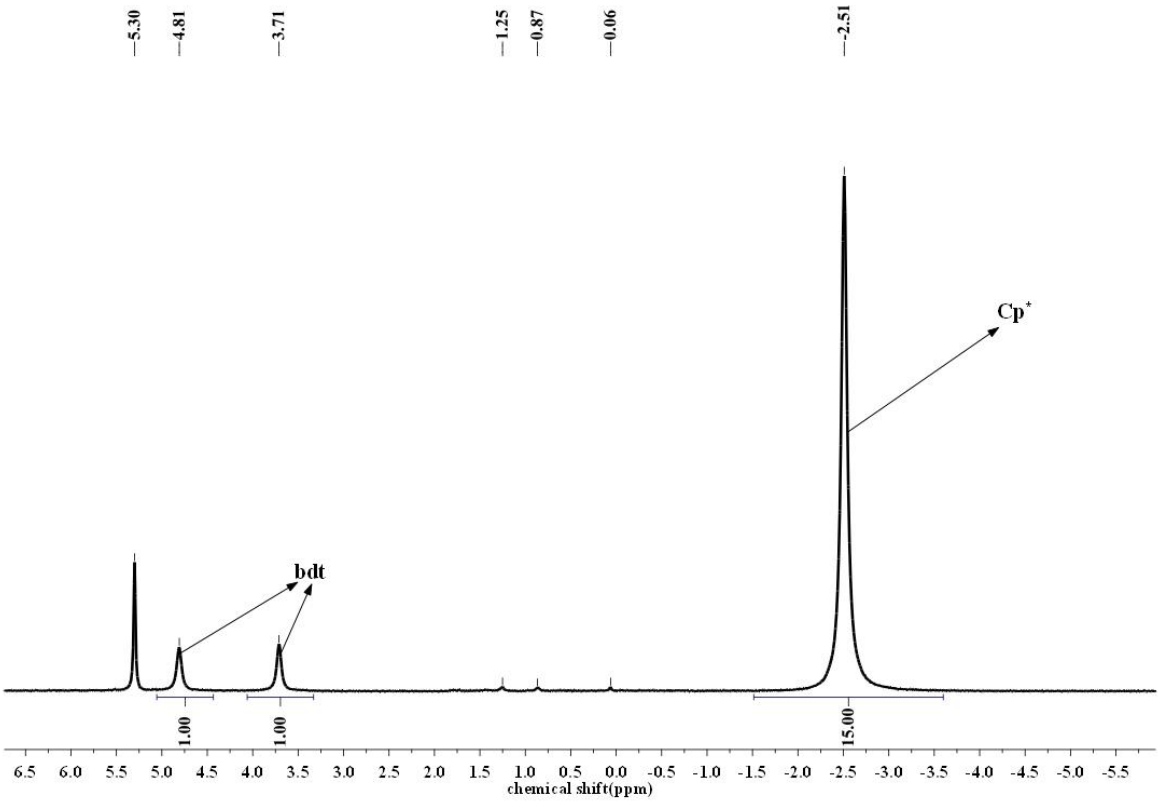

Figure S13. The various temperature ^{1}H NMR spectra of **3[BF_4]** in CD_2Cl_2

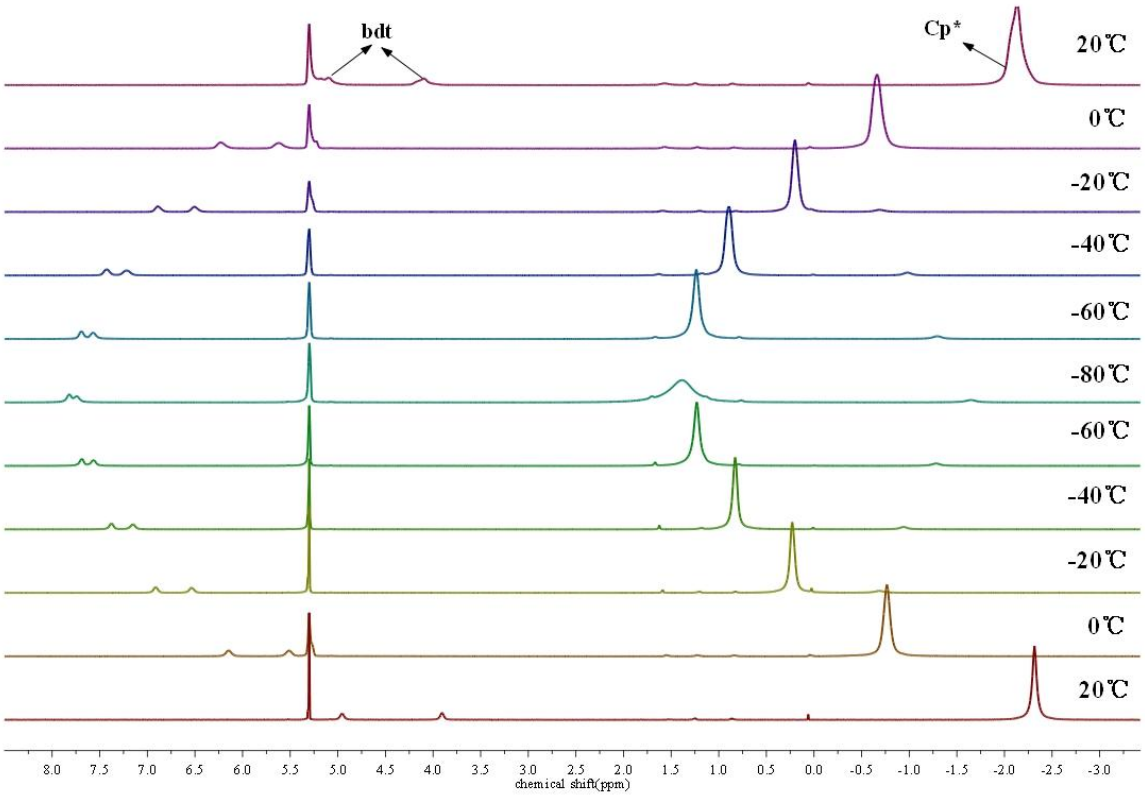

Figure S14. The ^{1}H NMR spectrum of **3[BPh_4]** in CD_2Cl_2

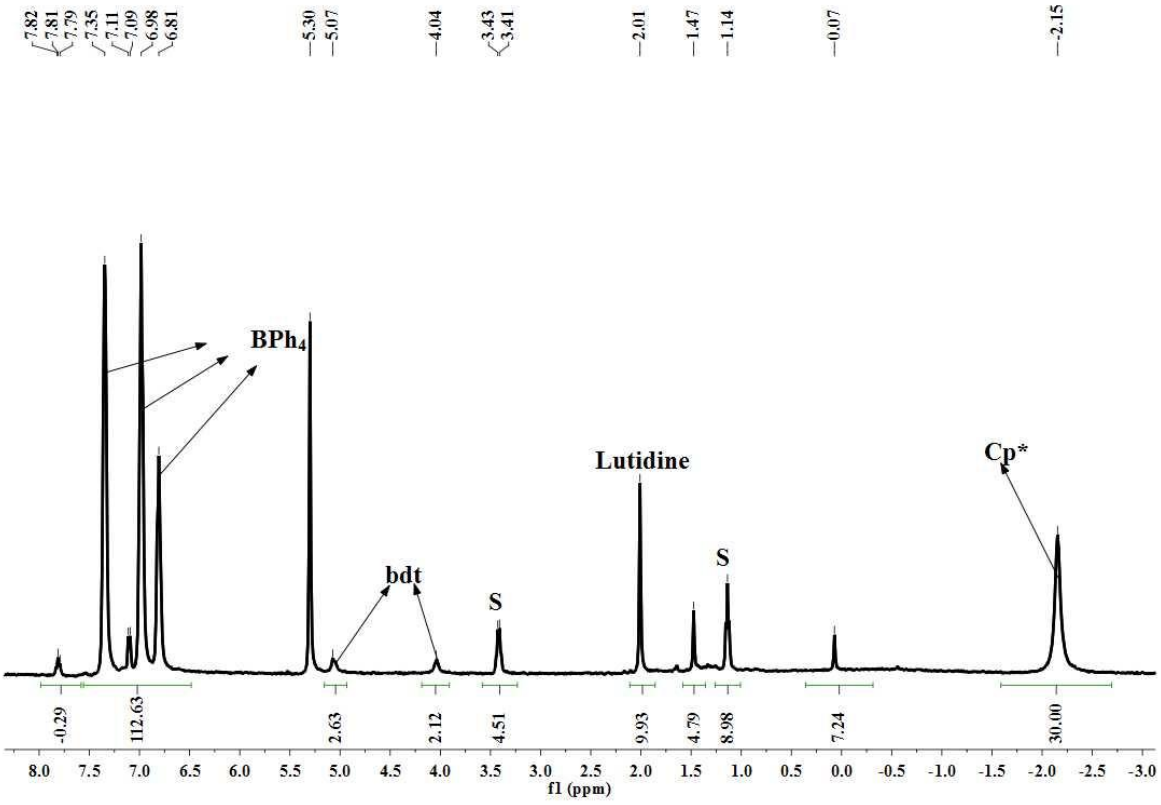

Figure S15. The ^{1}H NMR spectrum of **3[BAr$^F_4$]** in CD_2Cl_2

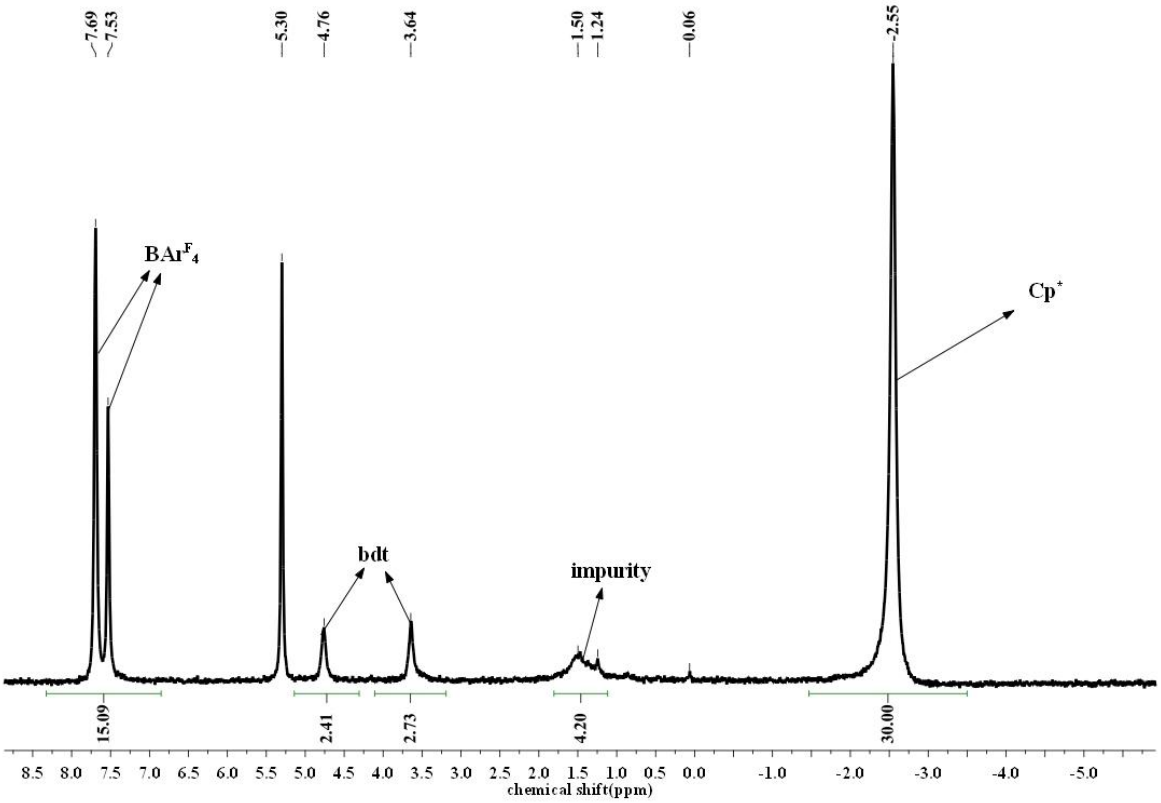

Figure S16. The ^{1}H NMR spectrum of **4** in CD_2Cl_2

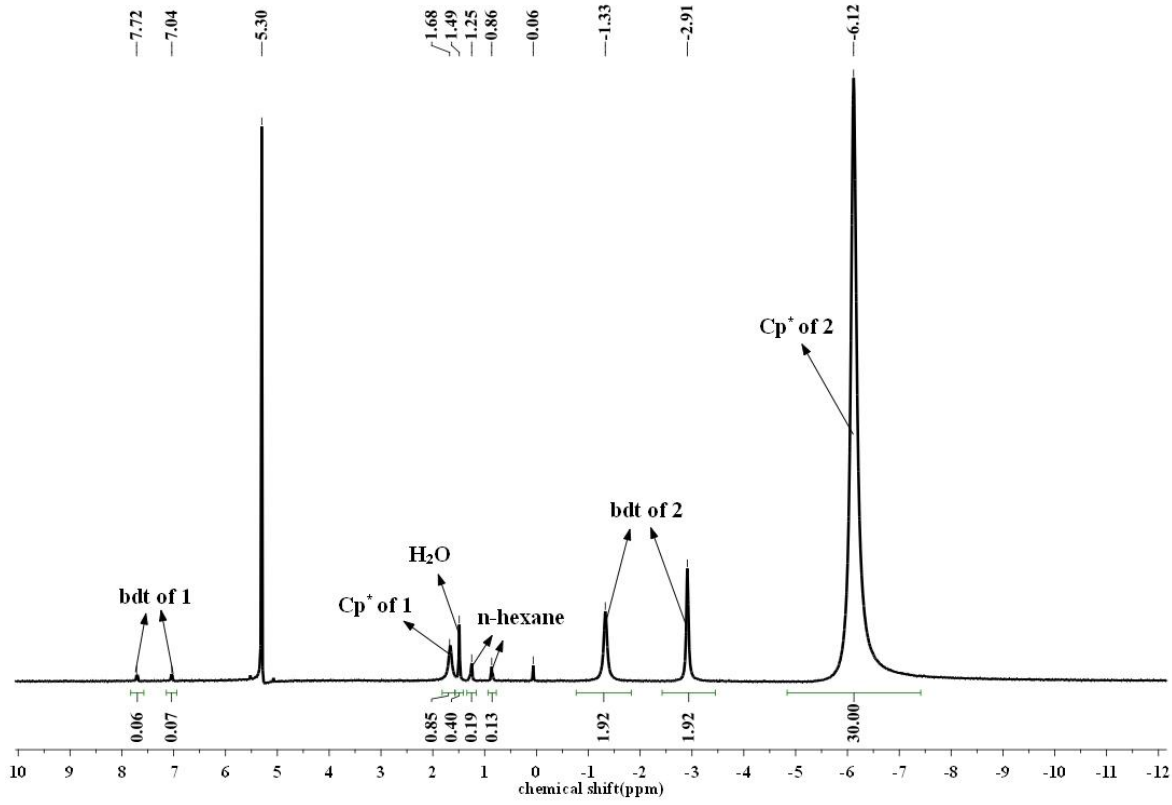

Figure S17. The various temperature ^{1}H NMR spectra of **4** in CD_2Cl_2

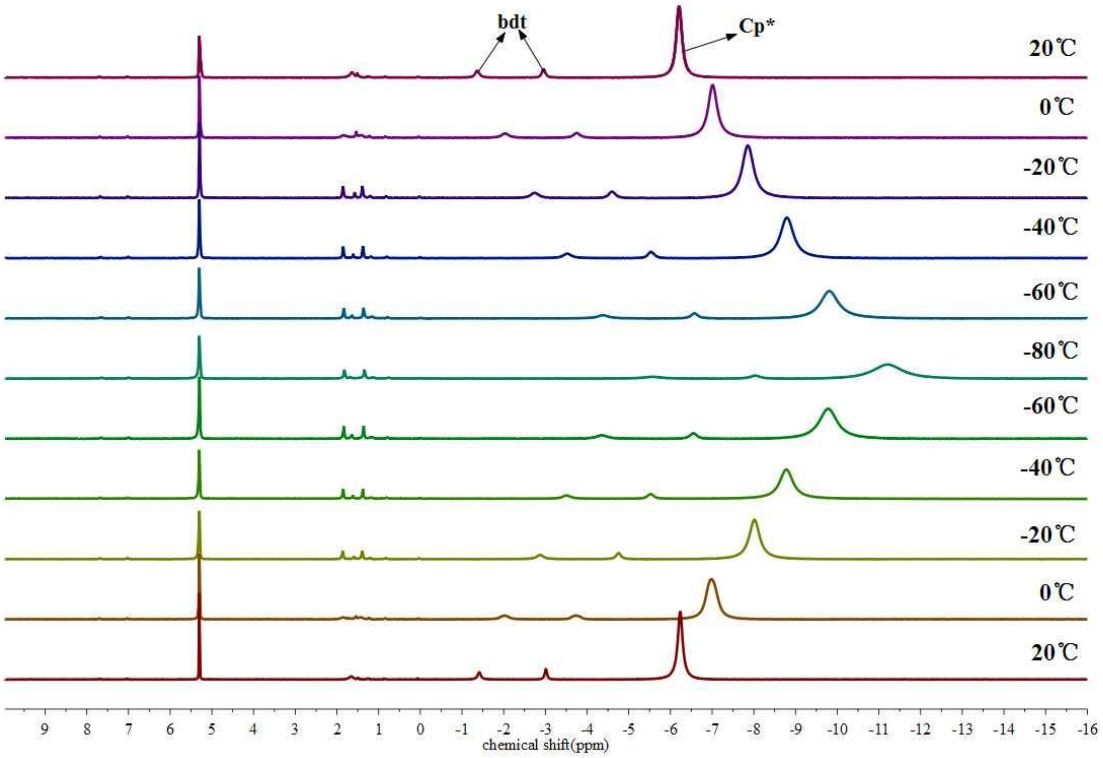

Figure S18. The ^{1}H NMR spectrum of **5** in CD_2Cl_2

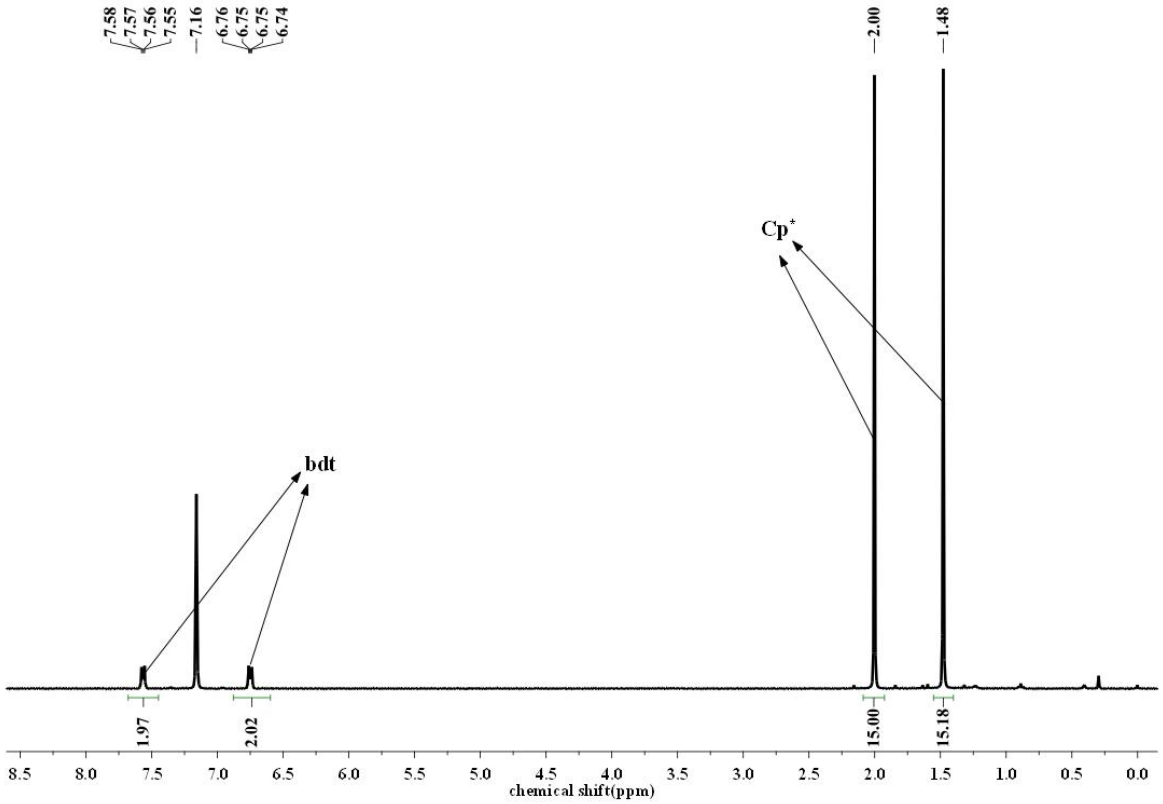

Figure S19. The ^{1}H NMR spectrum of **7[BF_4]** in CD_2Cl_2

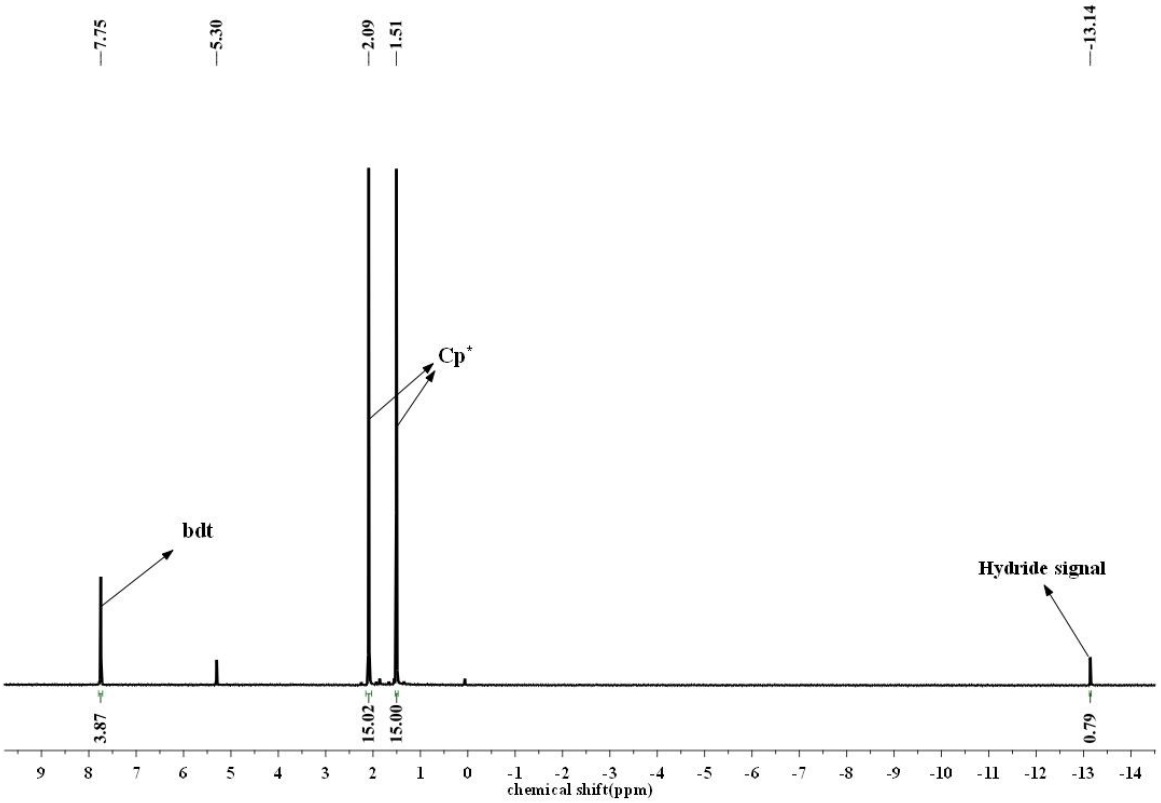

Figure S20. The ^{1}H NMR spectrum of **8[BF_4]** in CD_2Cl_2

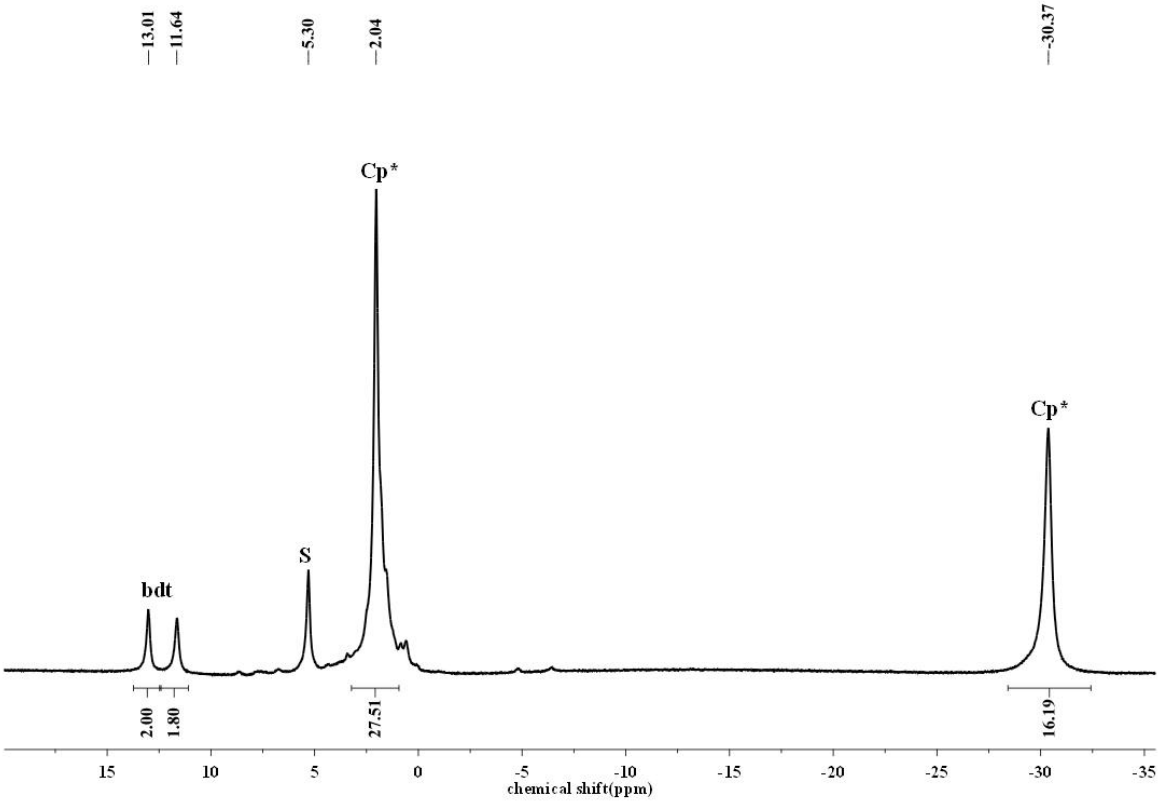

Figure S21. The ^{1}H NMR spectrum of **8** in CD_2Cl_2

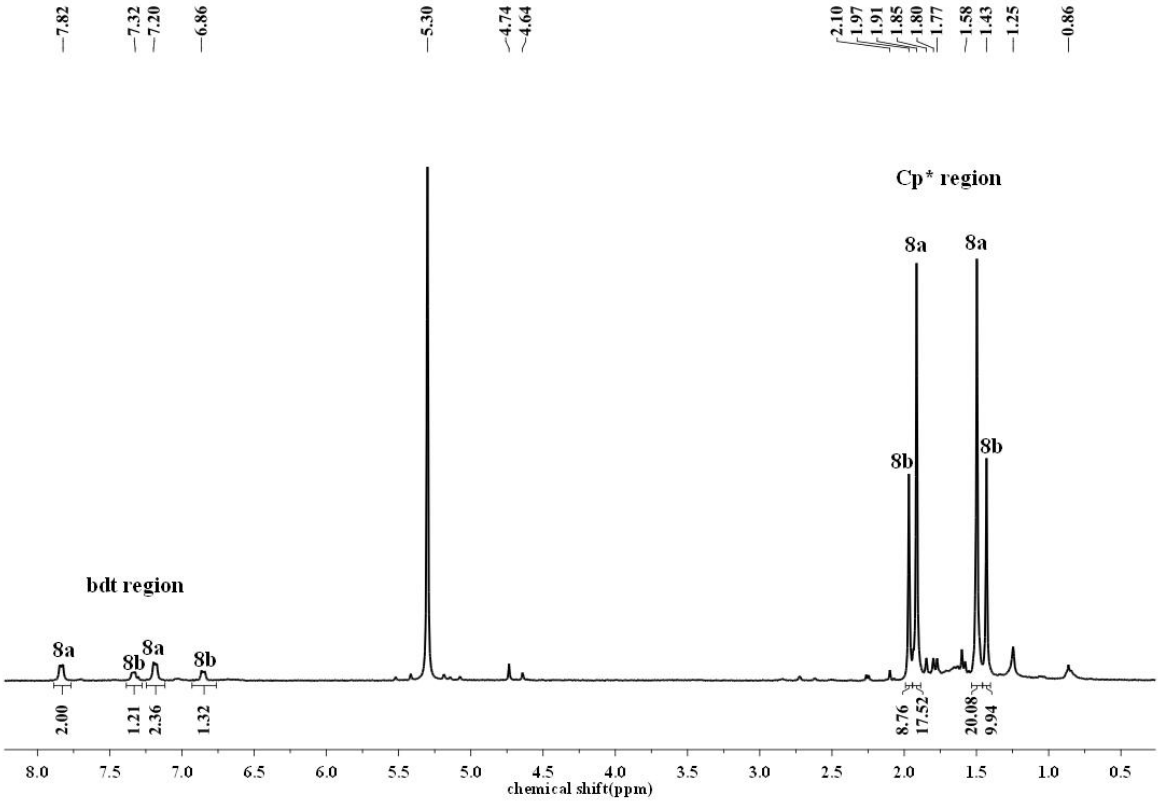

Figure S22. The IR (film) spectrum of **1[BF_4]**

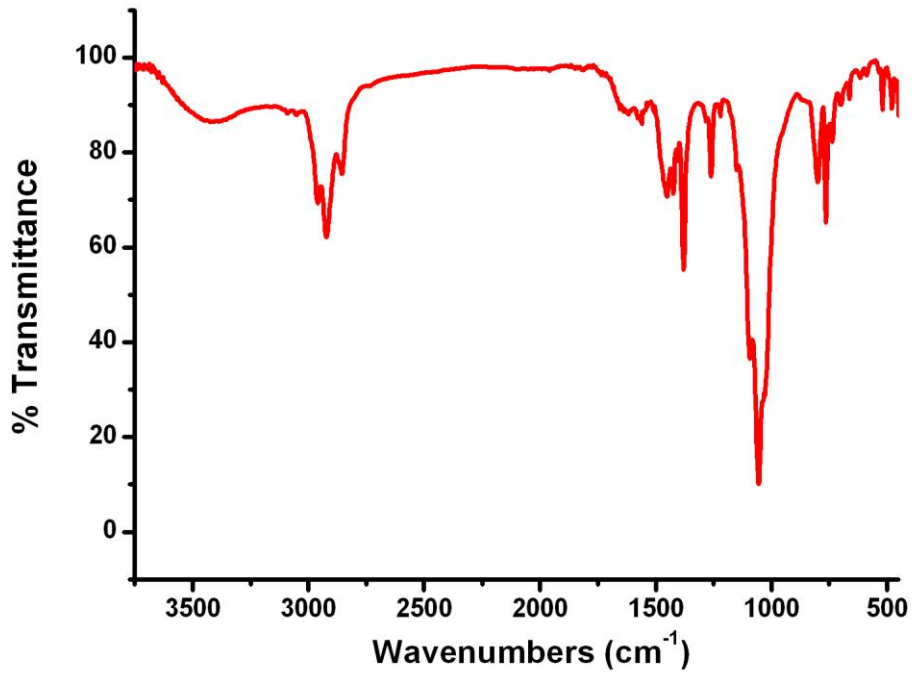

Figure S23. The IR (film) spectrum of **3[BF_4]**

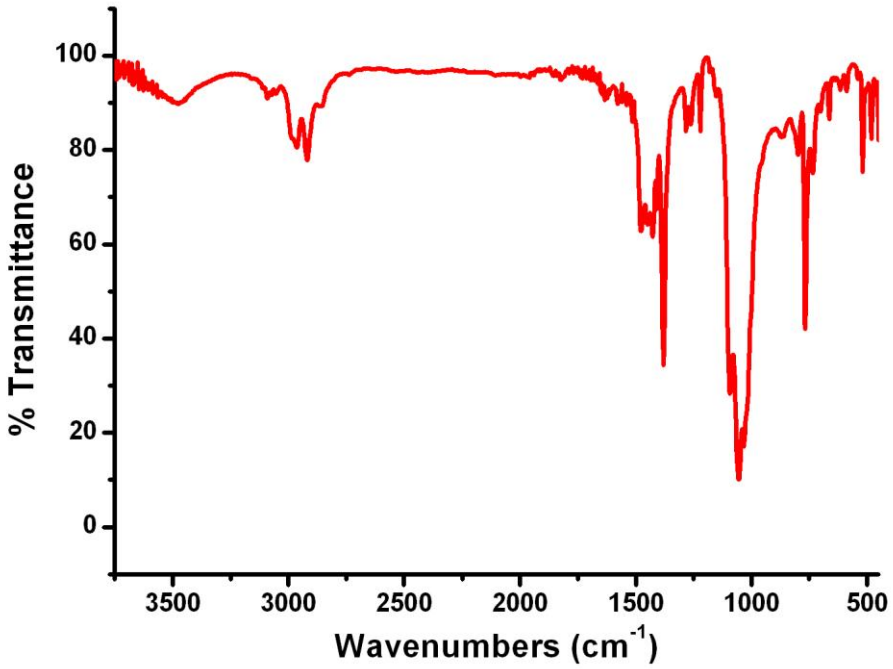

Figure S24. The IR (film) spectrum of **3[BPh_4]**

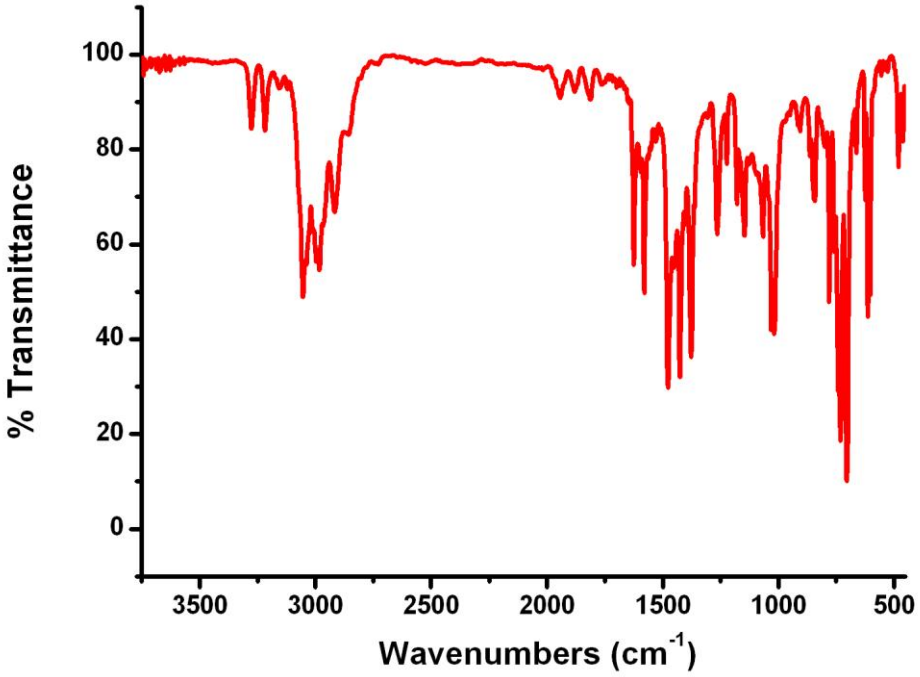

Figure S25. The IR (film) spectrum of **3[BAr$^{F}_{4}$]**

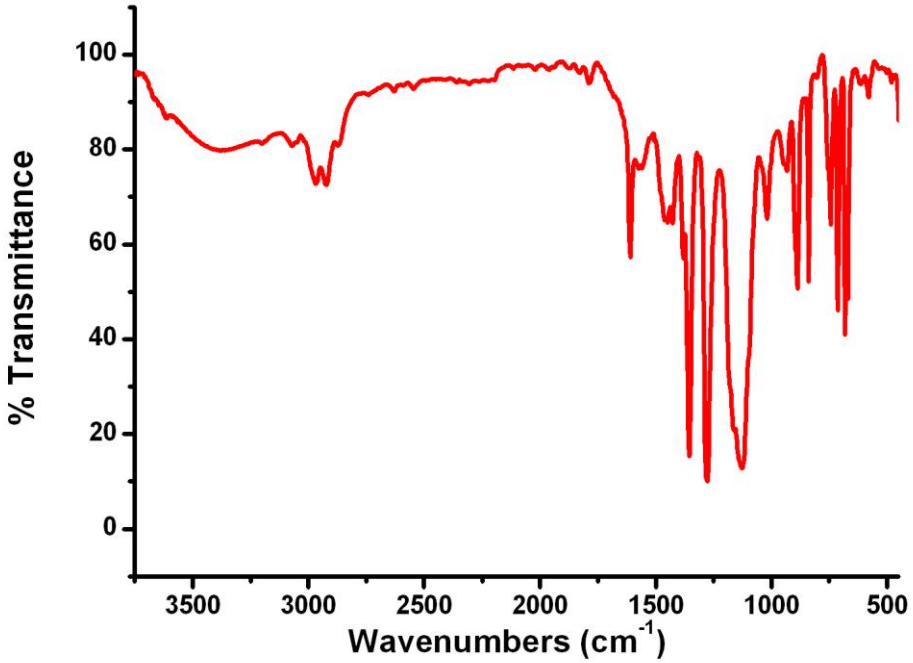

Figure S26. The IR (film) spectrum of **4**

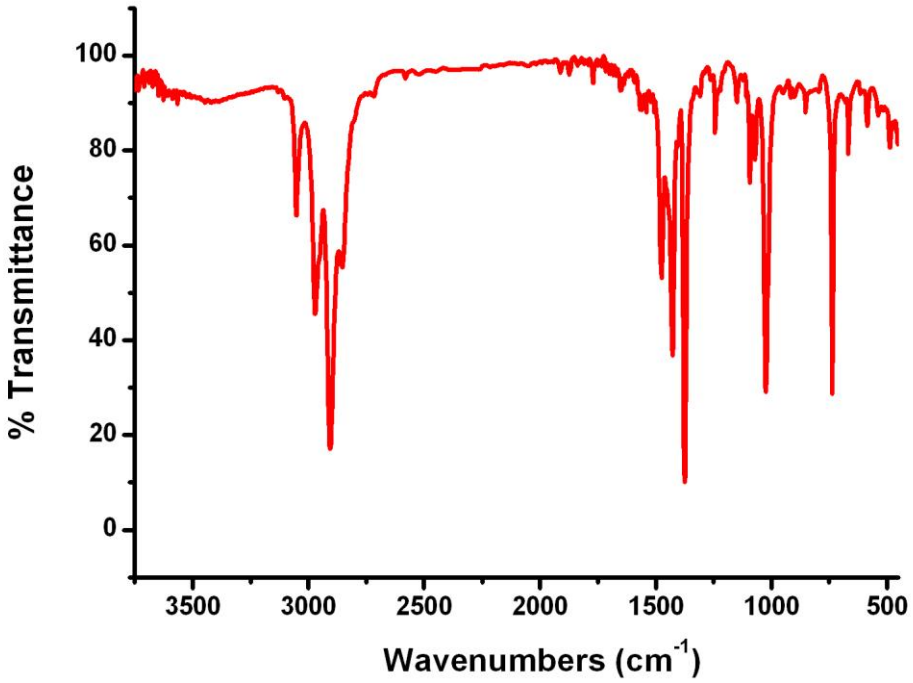

Figure S27. The IR (film) spectrum of **7[BF_4]**

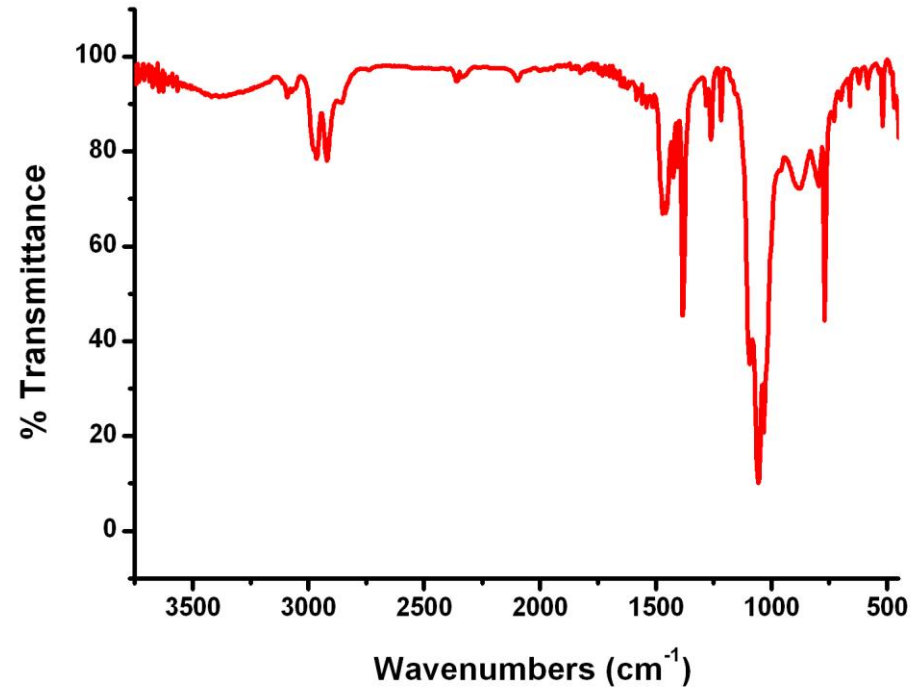

Figure S28. The IR (KBr) spectrum of **8[BF_4]**

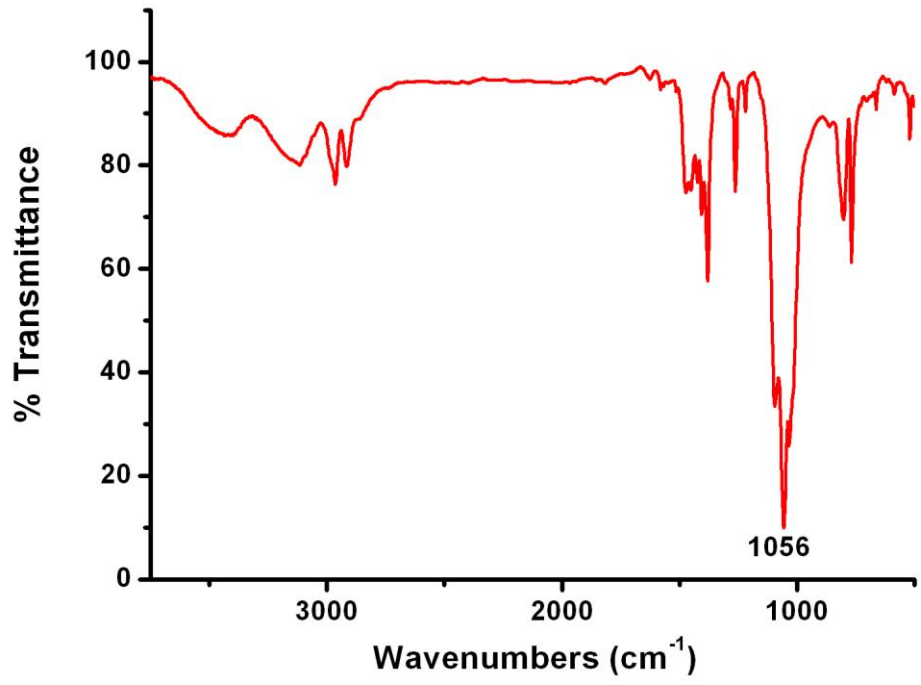

Figure S29. The IR (KBr) spectrum of **8**

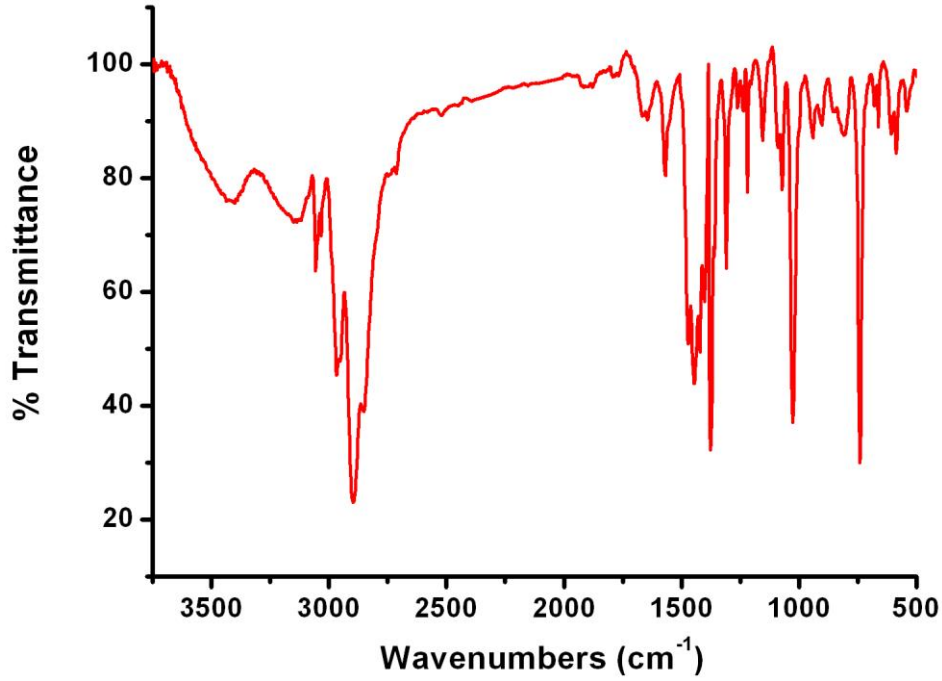

Figure S30. The μ_{eff} spectrum of **3[BF$_4$]**

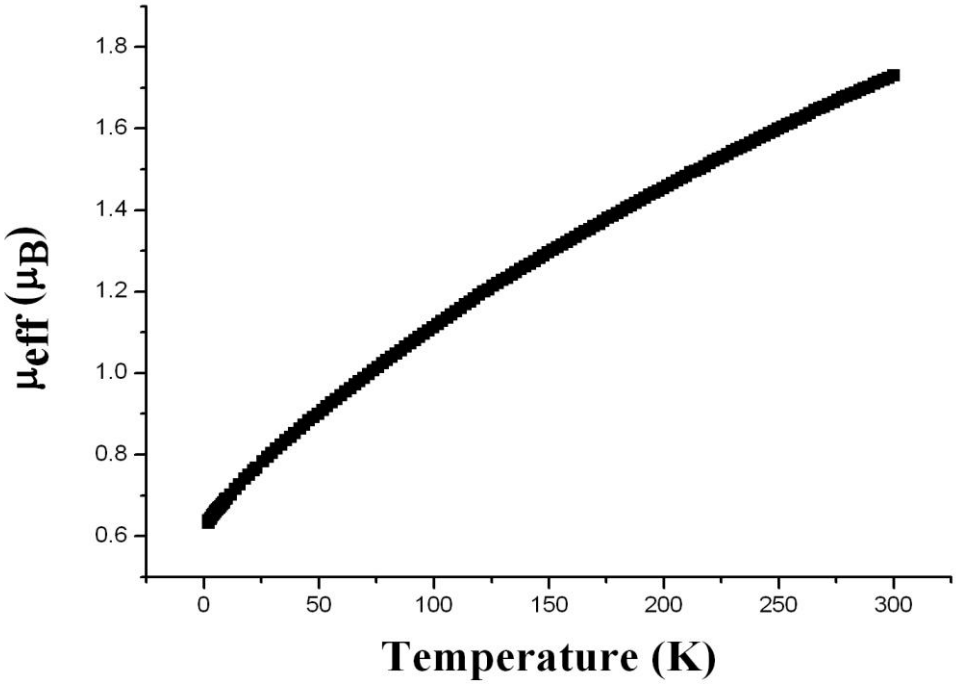

Figure S31. The μ_{eff} spectrum of **4**

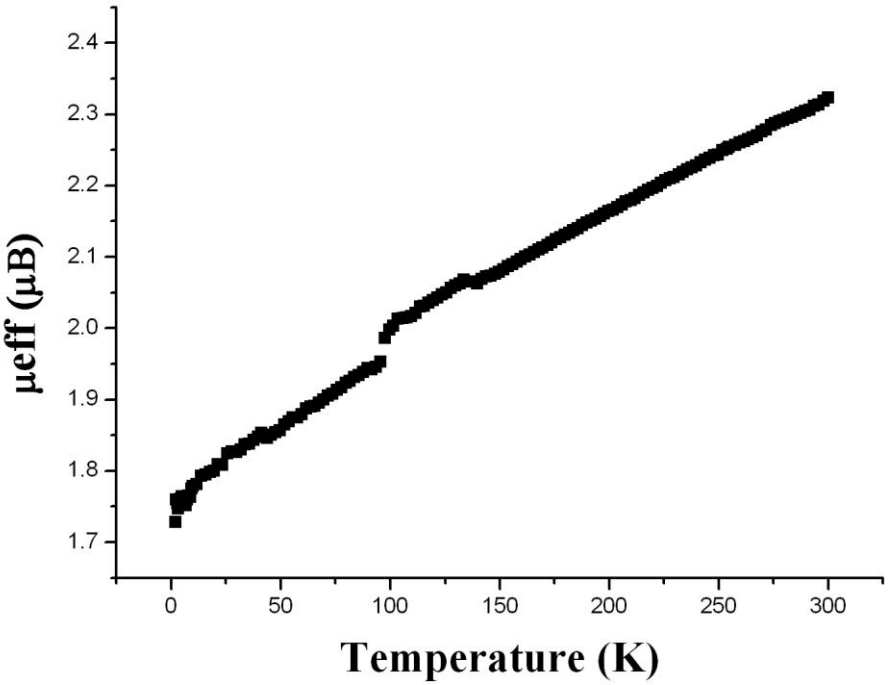

Figure S32. The *in situ* ^{1}H NMR spectra of protonation of **1** in CD_2Cl_2 (dark blue: terminal hydride complex **2**; dark red: hydride bridged complex **3[BF$_4$]**; dark green: **1[BF$_4$]**)

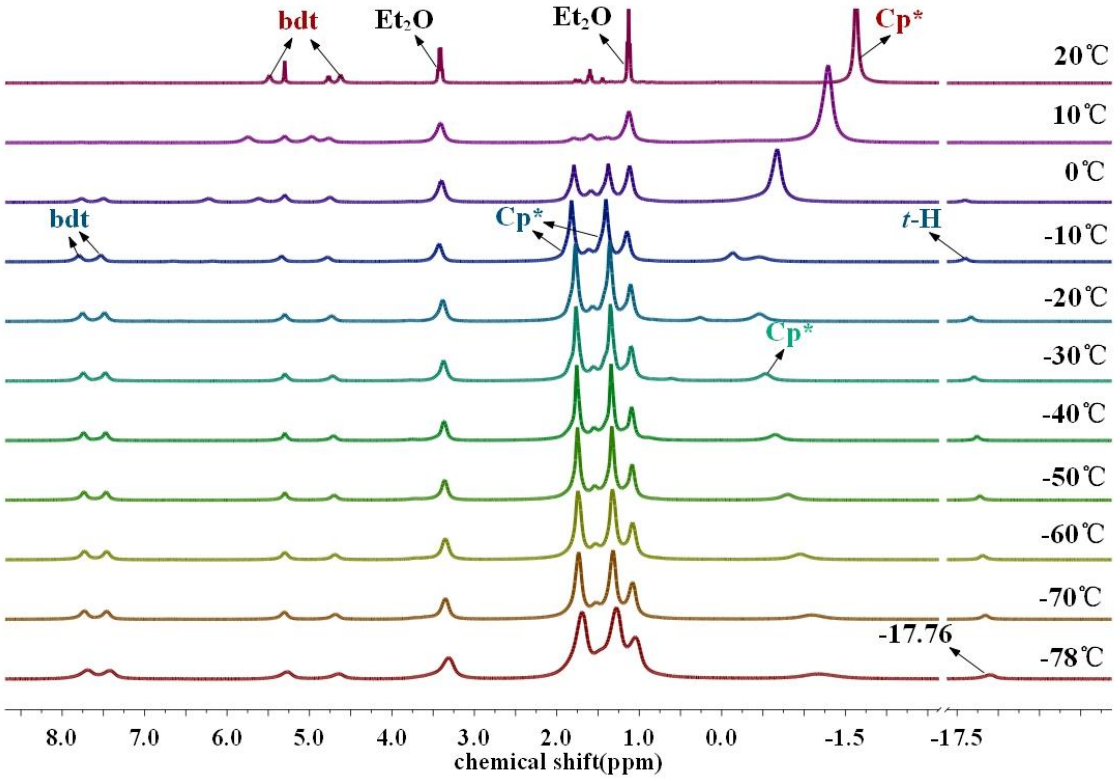

Figure S33. The *in situ* ^{1}H NMR spectra of protonation of **5** in CD_2Cl_2 (dark green: terminal hydride complex **6**; dark red: hydride bridged complex **7[BF_4]**)

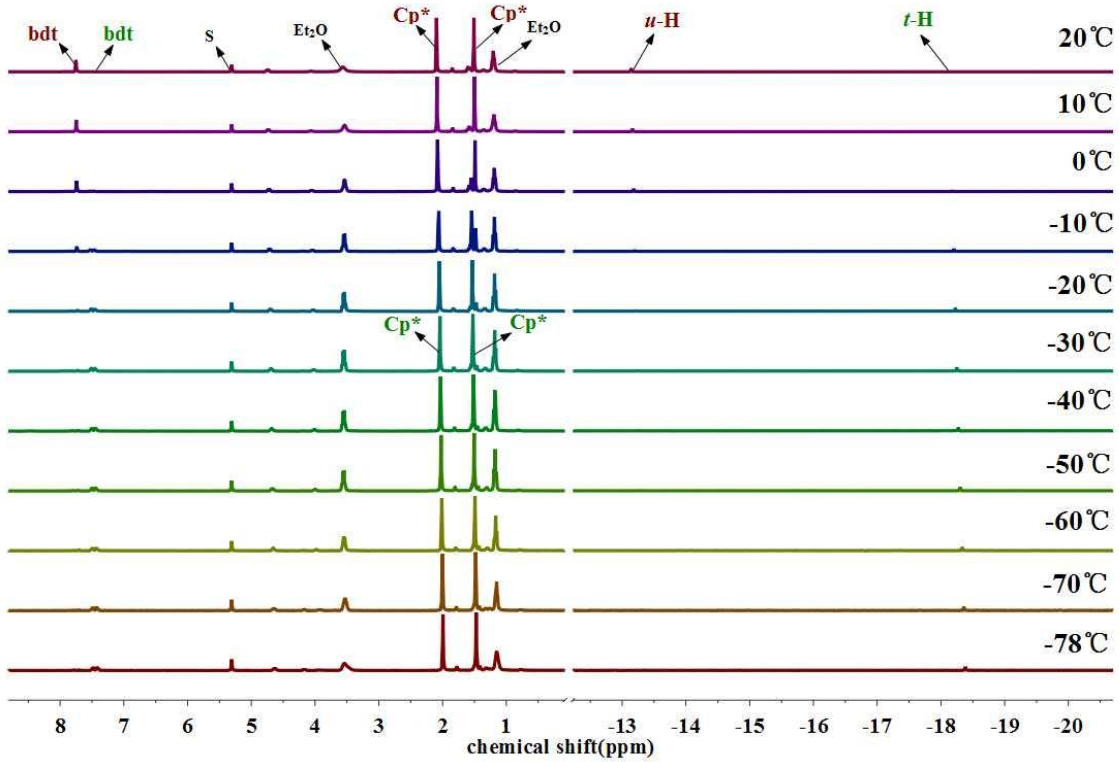

Figure S34. The hydride region of the *in situ* ^{1}H NMR spectra of protonation of **5** in CD_2Cl_2

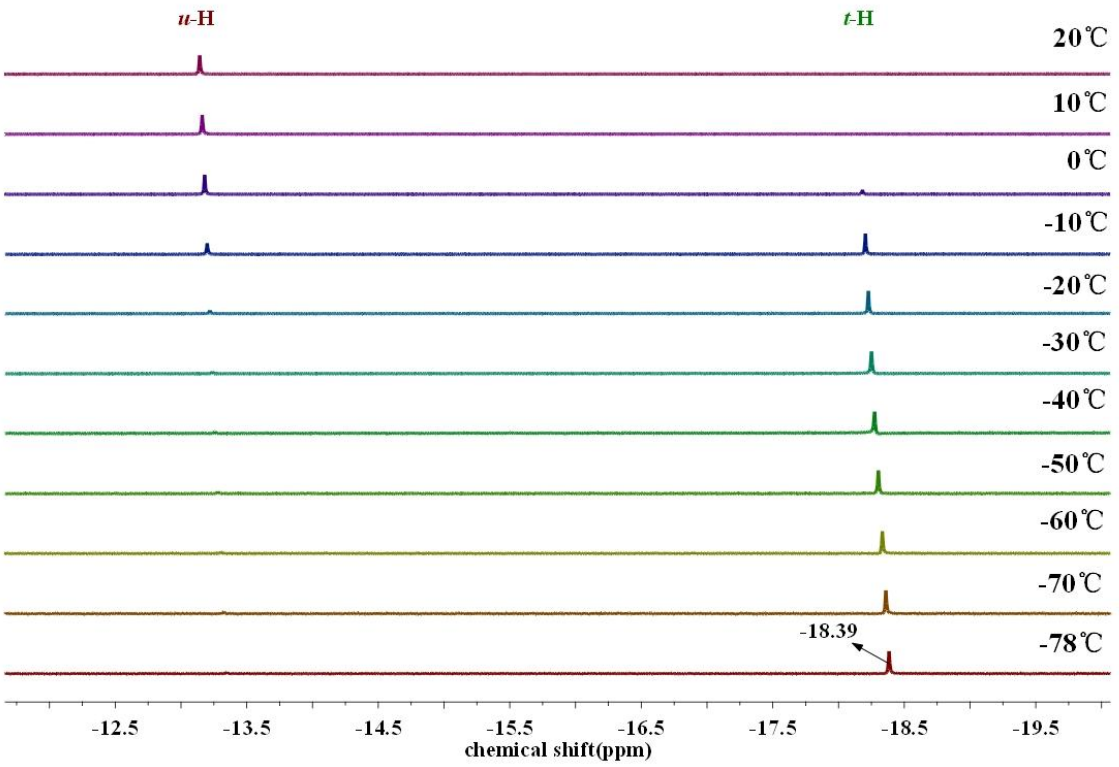

Figure S35. The *in situ* ^{1}H NMR spectra of protonation of **8** in CD_2Cl_2 (dark green: terminal hydride complex **9a** and **9b**; dark red: hydride bridged complex **10[BF_4]**)

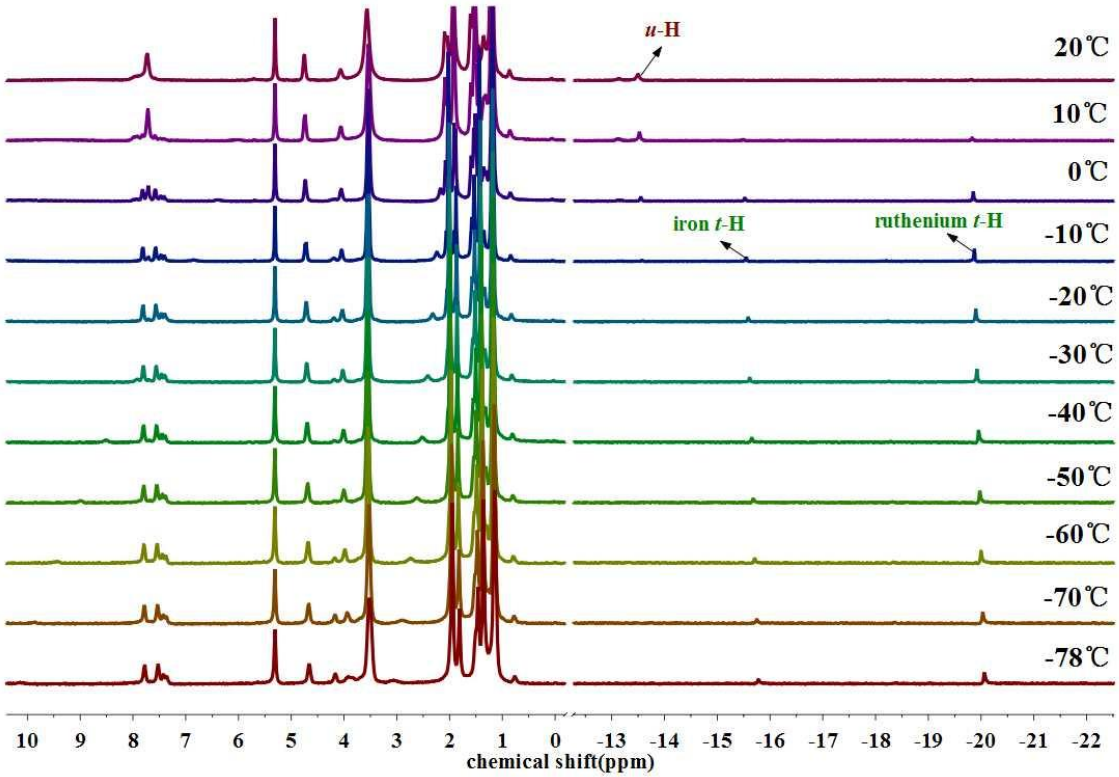

Figure S36. The hydride region of the *in situ* ^{1}H NMR spectra of protonation of **8** in CD_2Cl_2

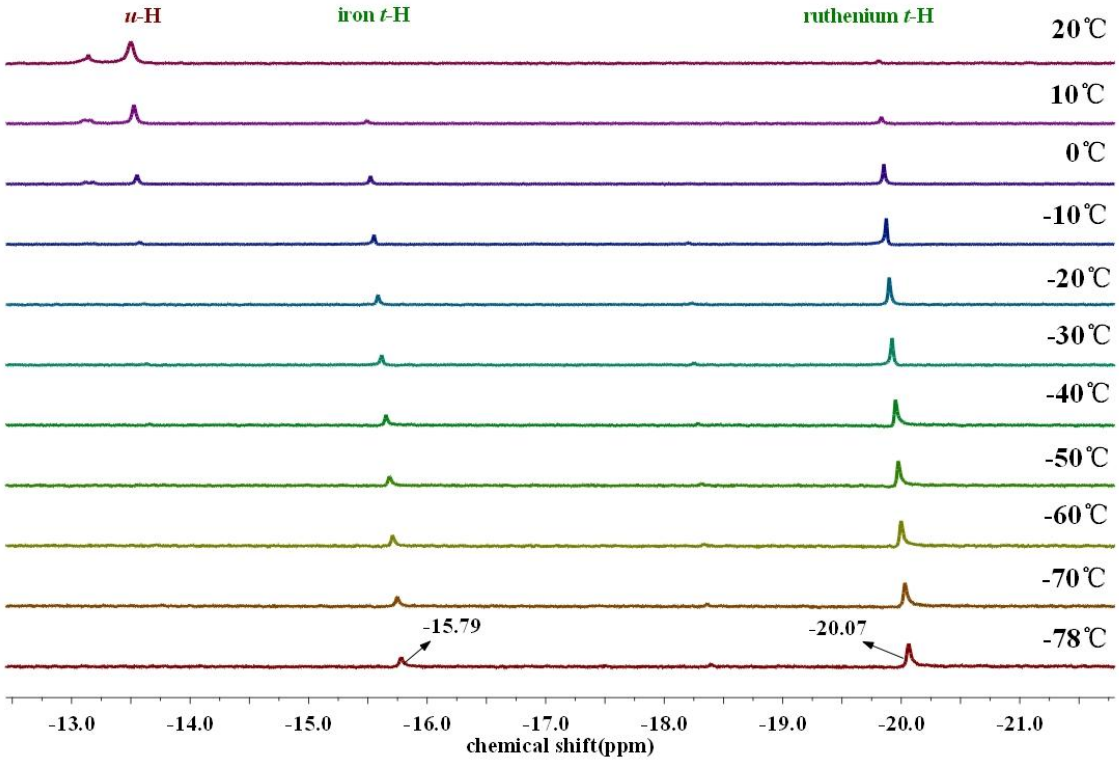

Figure S37. The cyclic voltammogram of **3[BF_4]** (1 mM) in 0.1 M $^{n}Bu_4NPF_6/CH_2Cl_2$ at 25 ^{o}C with a scan rate of 100 mV s^{-1}

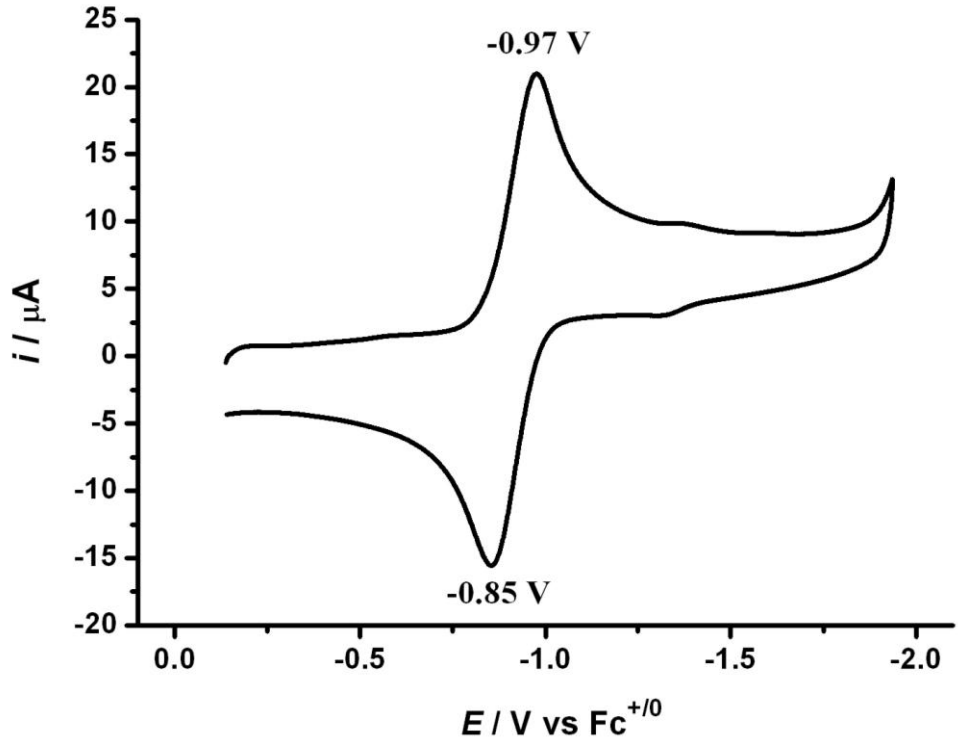

Figure S38. The cyclic voltammogram of **7[BF_4]** (1 mM) in 0.1 M $^{n}Bu_4NPF_6/CH_2Cl_2$ at 25 ^{o}C with a scan rate of 100 mV s^{-1}

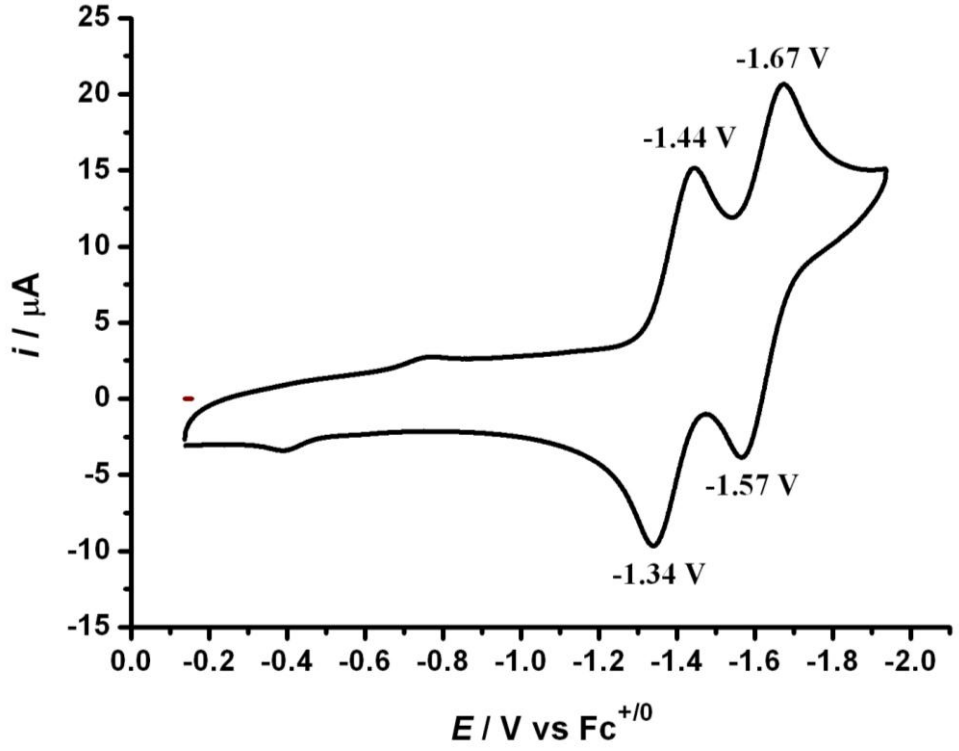

Figure S39. Cyclic voltammograms of **7[BF_4]** (1 mM in 0.1 M $^{n}Bu_4NPF_6$ in CH_2Cl_2 under Ar) with increments of HBF_4 (0, 1, 5, 10, 15, 20 mM)

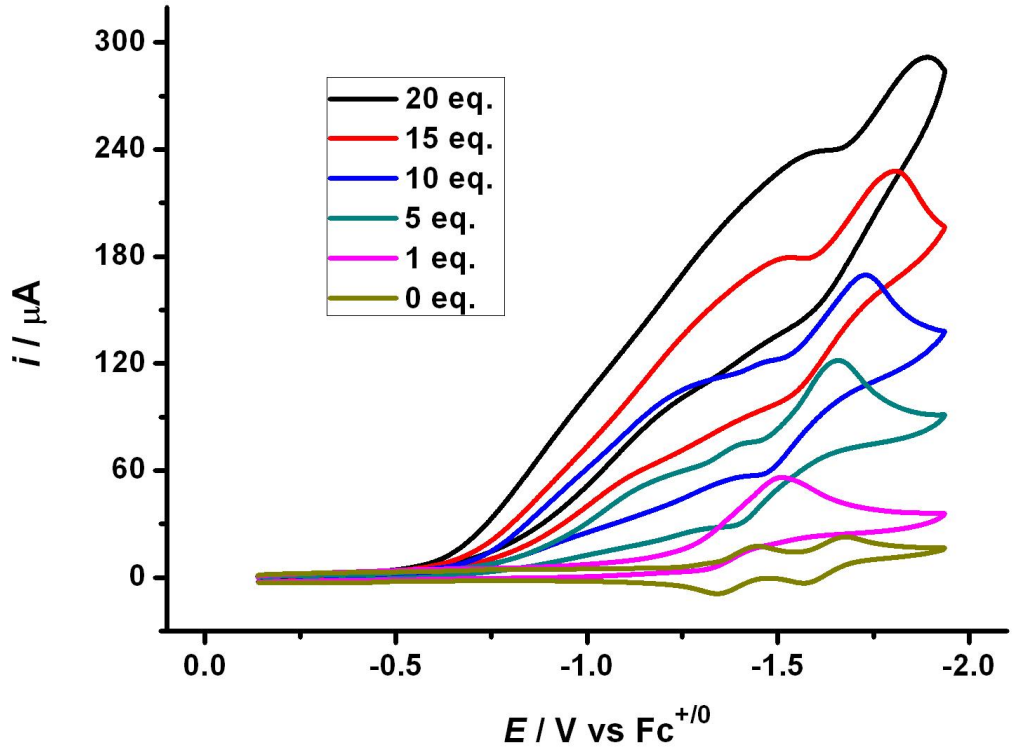

Figure S40. The cyclic voltammogram of **8[PF_6]** (1 mM) in 0.1 M $^{n}Bu_4NPF_6/CH_2Cl_2$ at 25 ^{o}C with a scan rate of 100 mV s^{-1}

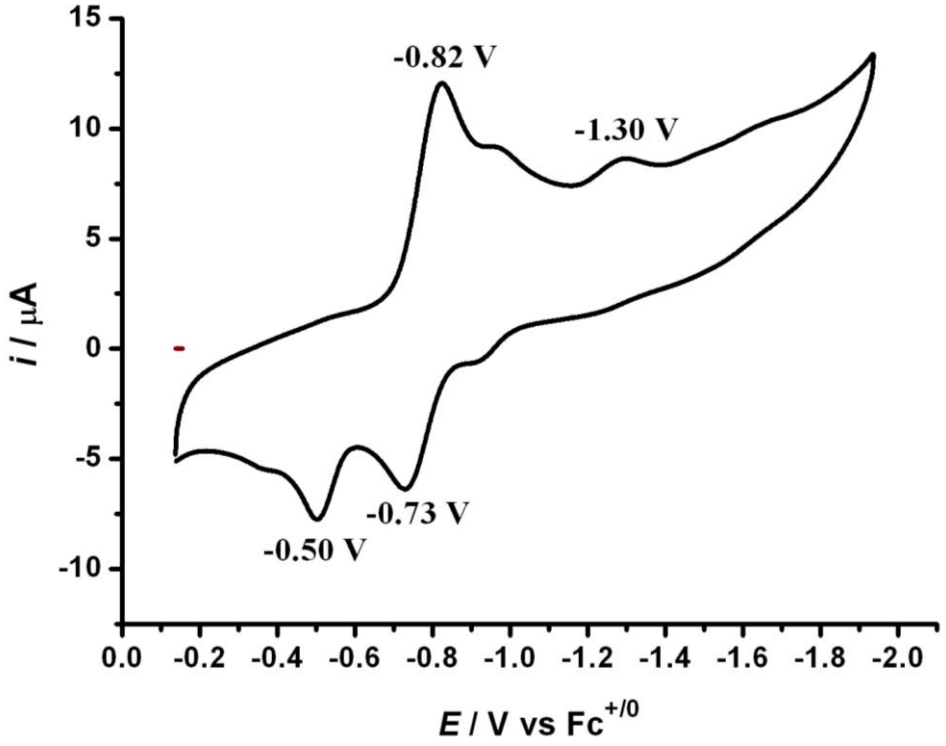

Figure S41. Cyclic voltammograms of **8[PF_6]** (1 mM in 0.1 M $^{n}Bu_4NPF_6$ in CH_2Cl_2 under Ar) with increments of HBF_4 (0, 1, 5, 10, 15, 20, 25, and 30 mM)

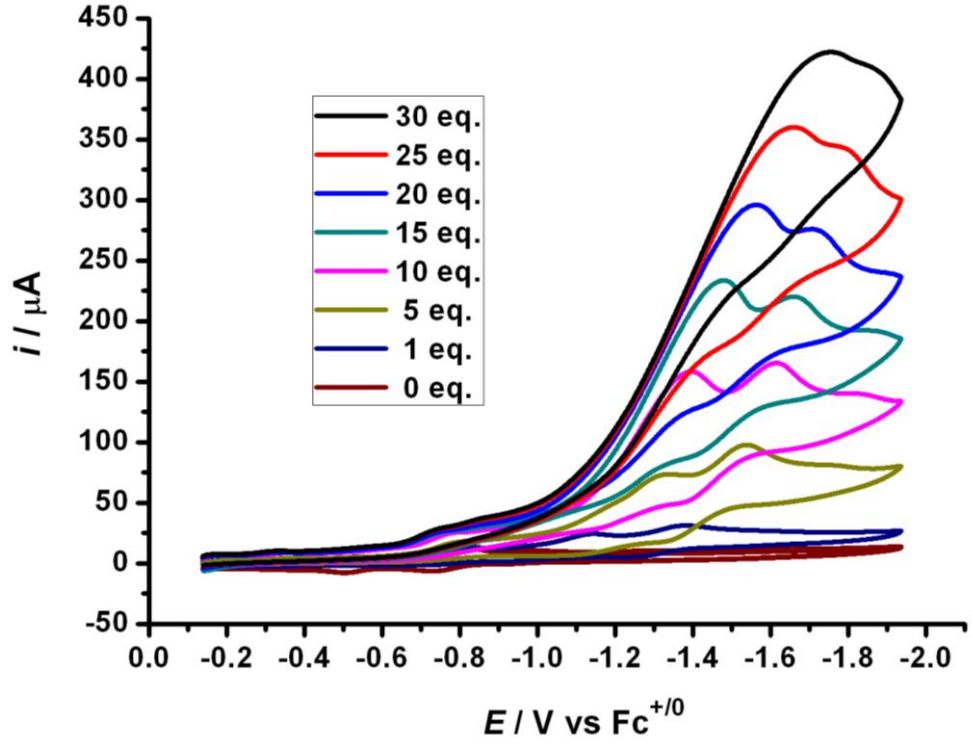

Figure S42. The dependence of the catalytic peak currents for 1 mM **3[BF_4]**, **7[BF_4]** and **8[PF_6]** on the concentration of HBF_4 in CH_2Cl_2

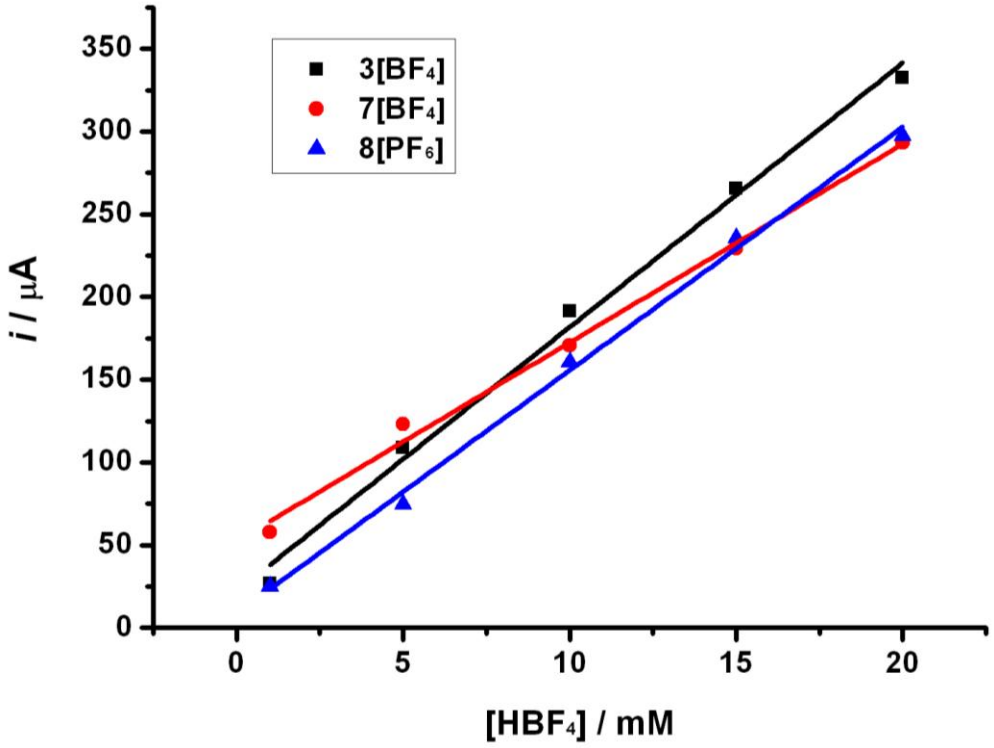

Figure S43. The cyclic voltammogram of 25 mM HBF_4 in 0.1 M $^{n}Bu_4NPF_6/CH_2Cl_2$ at 25 ^{o}C with a scan rate of 100 mV s^{-1}

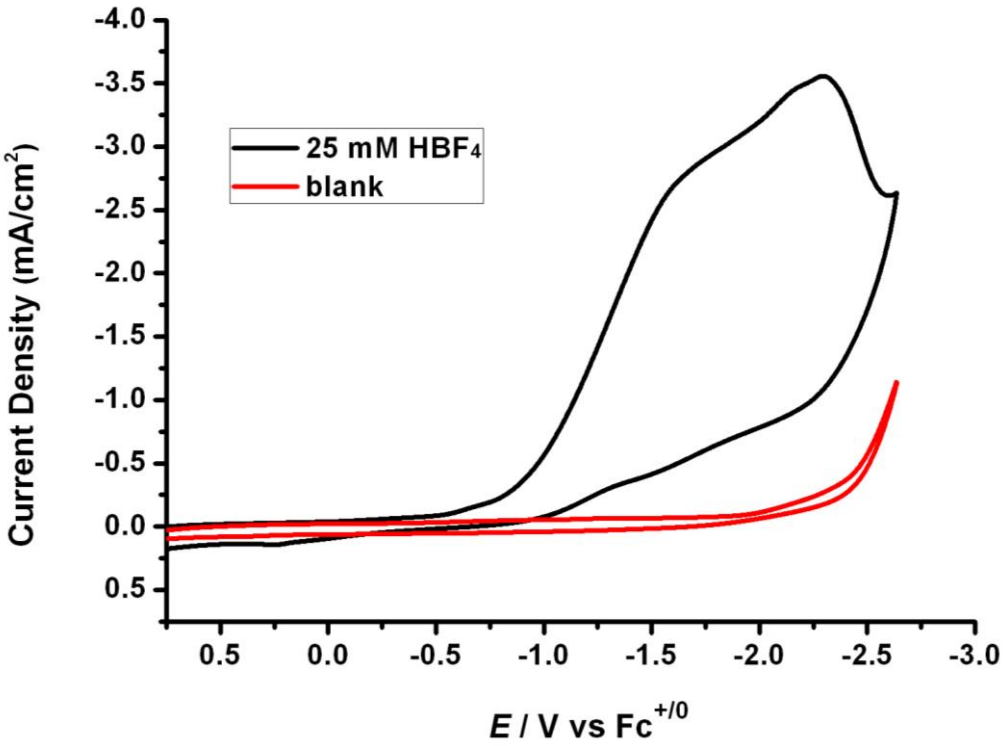

Figure S44. The cyclic voltammogram of **3[BF_4]** in the presence of 1 equivalent of HBF_4 in 0.1 M $^{n}Bu_4NPF_6/CH_2Cl_2$ at 25 ^{o}C with a scan rate of 100 mV s^{-1}

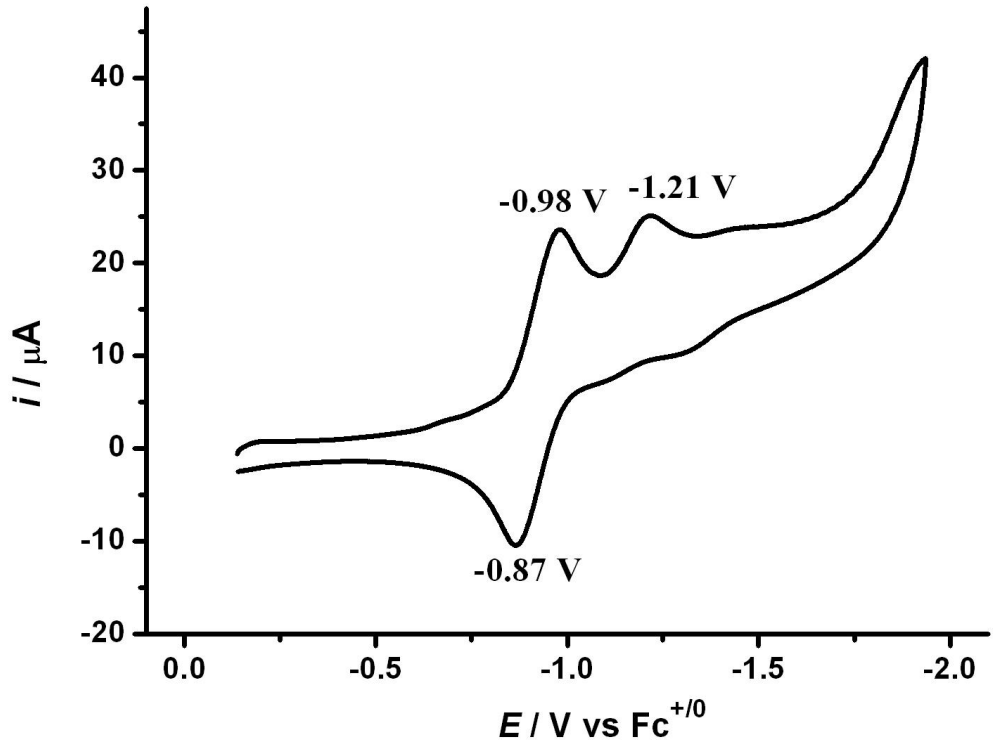

Figure S45. The i-t curve for bulk electrolysis of HBF_4 (30 mM) in the presence of **3[BF_4]** (1 mM) at −1.30 V

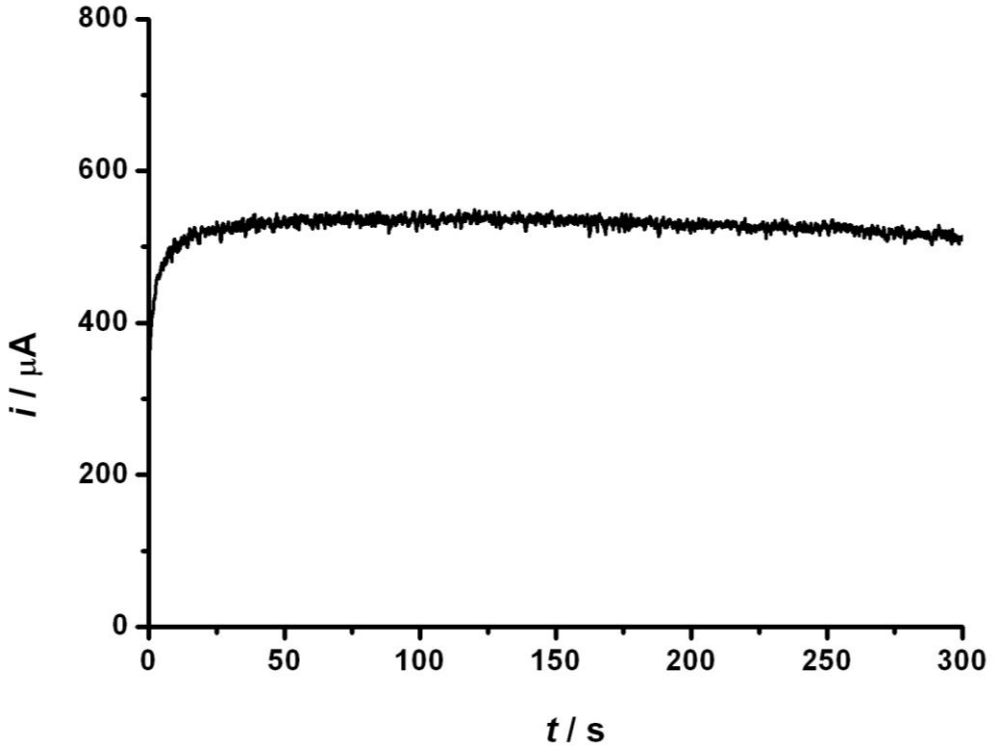

Figure S46. GC data for the three-electrode cell after electrolysis, the first peak at 0.687 min was ascribed to hydrogen.

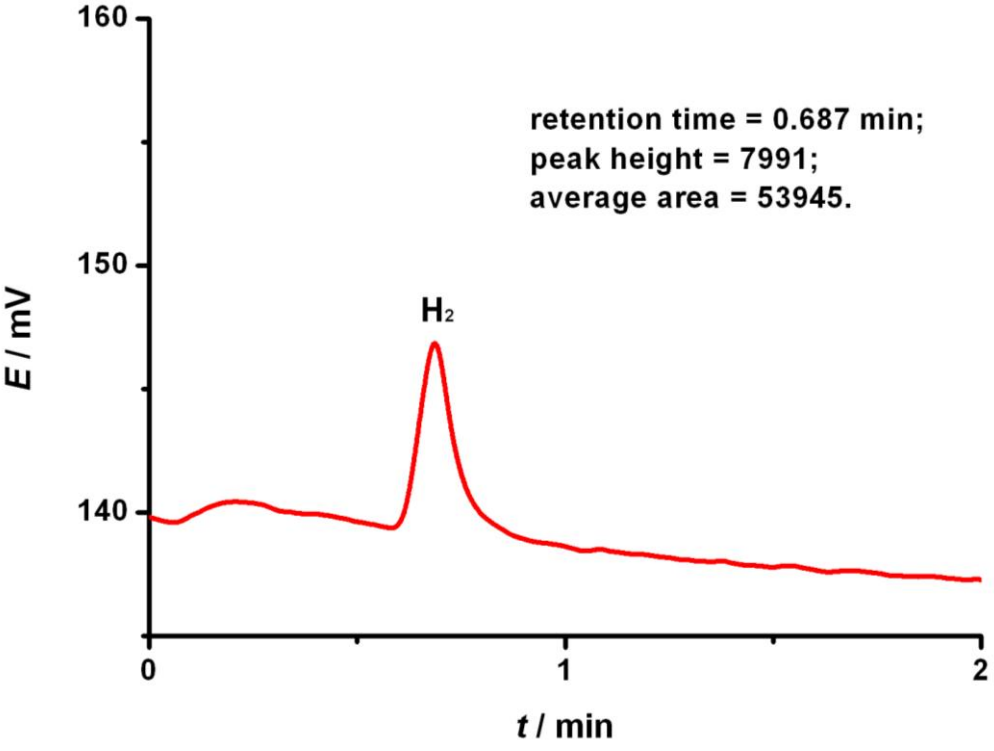

Figure S47. Two DFT-optimized structures of **3[BF_4]**

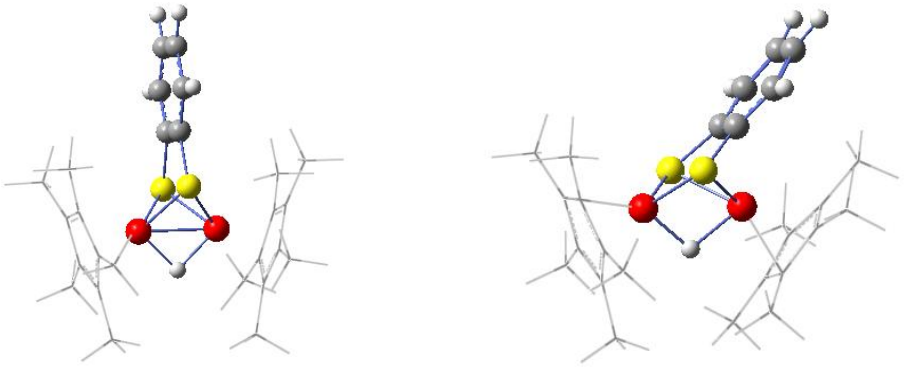

sym-3[BF_4] **unsym-3[BF_4]**

Table S9. Relative energy of **3[BF_4]** using TPSSTPSS density functional.

Complex	Spin multiplicity	Relative energy (kcal/mol)
sym-3[BF_4]	*S*=0	0.00
sym-3[BF_4]	*S*=1	−6.82
unsym-3[BF_4]	*S*=0	−10.63
unsym-3[BF_4]	*S*=1	−4.70